

Discontinuous Galerkin method for a three-dimensional coupled fluid-poroelastic model with applications to brain fluid mechanics

Ivan Fumagalli

MOX, Department of Mathematics, Politecnico di Milano, piazza Leonardo da Vinci 32, Milan, 20133, Italy

Abstract

The modeling of the interaction between a poroelastic medium and a fluid in a hollow cavity is crucial for understanding, e.g., the multiphysics flow of blood and Cerebrospinal Fluid (CSF) in the brain, the supply of blood by the coronary arteries in heart perfusion, or the interaction between groundwater and rivers or lakes. In particular, the cerebral tissue's elasticity and its perfusion by blood and interstitial CSF can be described by Multi-compartment Poroelasticity (MPE), while CSF flow in the brain ventricles can be modeled by the (Navier-)Stokes equations, the overall system resulting in a coupled MPE-(Navier-)Stokes system. The aim of this paper is three-fold. First, we aim to extend and verify in a three-dimensional setting a discontinuous Galerkin method on polytopal grids recently presented for the MPE-Stokes problem. Second, we carry out the analysis of the method based on an extension of the proposed formulation so that physics-based Beavers-Joseph-Saffman conditions are taken into account at the interface: these conditions are essential to model the friction between the fluid and the porous medium. Finally, by a comparative numerical investigation, we assess the fluid-dynamics effects of these boundary conditions and of employing either Stokes or Navier-Stokes equations to model the CSF flow. The semidiscrete numerical scheme for the coupled problem is proved to be stable and optimally convergent. Temporal discretization is obtained using Newmark's β -method for the elastic wave equation and the θ -method for the remaining equations of the model. The theoretical error estimates are verified by numerical simulations on a test case with a manufactured solution, and a numerical investigation is carried out on a three-dimensional geometry to assess the effects of interface conditions and fluid inertia on the system.

Keywords – Navier-Stokes equations, Multiple-network Poroelasticity Theory, Beavers-Joseph-Saffman interface conditions, Polyhedral mesh, Cerebrospinal fluid

1 Introduction

Many mathematical models of interest in the applications entail the coupling between a poroelastic medium and a fluid flowing in a hollow region outside of the matrix pores: it is the case, e.g., of the interaction between groundwater and surface waterbodies [1, 2], between the blood-perfused cardiac tissue and the coronary flow [3, 4], or between the interstitial Cerebrospinal Fluid (CSF) in the brain tissue and its flow in the hollow cerebral ventricles [5, 6]. The latter is particularly relevant in the modeling of the waste clearance function played by CSF in the development of neurodegenerative diseases such as Alzheimer's [7, 8]. Moreover, the CSF flow is strongly interconnected with the pulsatility of blood in the cerebral vasculature and capillaries [5, 9], thus requiring for a Multiple-network Poroelasticity (MPE) model to account for the interstitial CSF and the blood flowing at different spatial scales in the porous tissue [10, 11].

From the standpoint of finite element literature, interest has been paid to fluid-dynamics and poromechanics problems with the development and analysis of several methods, especially in the Discontinuous Galerkin (DG) class, including interior-penalty DG [12, 13, 14, 15], staggered DG [16, 17, 18], and hybrid DG [19, 20, 21]. The coupling of the fluid and poroelastic systems yields a complex multi-physics problem, investigated in the numerical literature in the case of the Biot-Stokes model [22, 23, 24, 25], also in the regime of large deformations [26], or for multilayered porous media coupled with Newtonian fluid flows [27, 28]. However, almost no numerical analysis of the discretization of fluid-poromechanics equations with multiple porous compartments can be found in the literature, despite their relatively wide use in the applications [4, 29, 30]: the MPE system - without a coupled fluid problem - has been analyzed in [31, 32, 11], but the numerical analysis of the coupled MPE-Stokes problem can be found only in [33]. In the case of applications to brain function, the main challenges are the high complexity of the domain (encompassing intricate folds and tortuous channels) and the paramount role of stress and flow exchanges at the interface between the two physical domains. Therefore, a particularly suitable choice is the use of the Polytopal Discontinuous Galerkin (PolyDG) method, for three reasons:

- by supporting general mesh element shapes, it exhibits strong geometrical flexibility and it allows local refinement and hanging nodes;
- high-order polynomials can be naturally employed in the discretization, thus guaranteeing low dispersion and dissipation errors, which is particularly relevant at the physical interface;
- interface conditions can be naturally incorporated in the formulation, thanks to element-wise integration by parts.

In this framework, the present work has three aims:

- expanding and verifying the PolyDG method proposed in [33] in three-dimensional geometries;
- extending the numerical method to include the physically-motivated Beavers-Joseph-Saffman (BJS) interface conditions and analyzing the stability and convergence of the resulting scheme. The BJS conditions play an essential role in practical applications, like in brain fluid mechanics or groundwater flows, because they take into account the friction and relative tangential velocity between the porous medium and the fluid in contact with it [34, 6];
- assessing the fluid-dynamics effects of modeling the CSF by either Stokes or Navier-Stokes equations, in the aforementioned multi-physics scenario and in the typical regime of brain waste clearance. Both fluid models have been used in the literature, but a direct quantitative comparison between the two is missing.

The paper is organized as follows. Section 2 describes the multiphysics mathematical model and its weak formulation, particularly discussing the imposition of interface conditions. The PolyDG space discretization method is introduced in Section 3 and its stability and convergence analysis is presented in Section 4. Time discretization is introduced in Section 5, while Section 6 reports some verification tests. Numerical results in a physiological regime are discussed in Section 7, while Section 8 reports an assessment of the impact of the BJS condition and the advection term in Navier-Stokes equations on CSF flow and intracranial pressure.

2 Mathematical model

We consider the coupling of a Multiple-Network Poroelasticity system and Navier-Stokes equations in a domain such as the one displayed in Fig. 1. The overall domain $\Omega \in \mathbb{R}^d$ ($d = 2, 3$) is split into a poroelastic region Ω_{el} and a fluid region Ω_{f} , separated by the interface $\Sigma = \overline{\Omega_{\text{el}}} \cap \overline{\Omega_{\text{f}}}$, which is assumed to be a piecewise smooth $(d - 1)$ -manifold. The poroelastic region is filled by an elastic solid body and N_J fluid components, indicated by the elements of an index set J . Within this set, let us assume that only one component directly exchanges mass through Σ : we denote this component by $E \in J$. The displacement of the solid matrix is denoted by $\mathbf{d} : \Omega_{\text{el}} \rightarrow \mathbb{R}^d$, its corresponding stress tensor is $\sigma_{\text{el}}(\mathbf{d}) = 2\mu_{\text{el}}\varepsilon(\mathbf{d}) + \lambda(\nabla \cdot \mathbf{d})I$, with $\varepsilon(\mathbf{d}) = \frac{1}{2}(\nabla \mathbf{d} + \nabla \mathbf{d}^T)$, and each of the fluid components is characterized by a pressure $p_j : \Omega_{\text{el}} \rightarrow \mathbb{R}, j \in J$. In the fluid domain Ω_{f} , velocity, pressure, and viscous stress are denoted by $\mathbf{u}, p,$

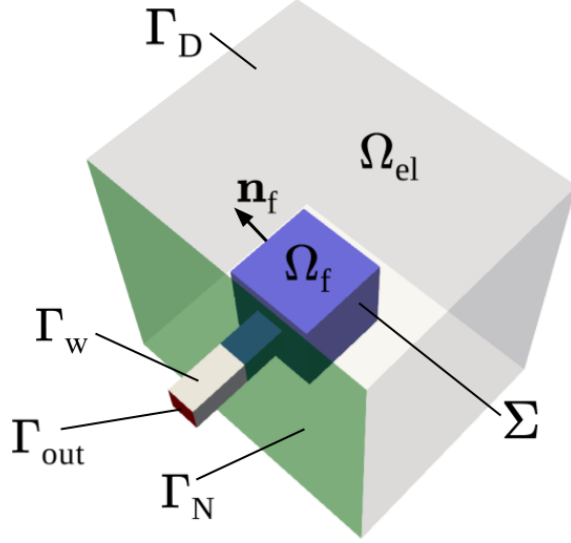


Figure 1: Computational domain: poroelastic region Ω_{el} and fluid region Ω_f , interface Σ between them (blue), and external boundaries Γ_{out} (red), Γ_w (grey), Γ_D (light grey) and Γ_N (green).

and $\tau_f(\mathbf{u}) = 2\mu_f \varepsilon(\mathbf{u})$, respectively. The physical parameters in the above definitions and in the following are assumed to be constant.

At the fluid-poroelastic interface Σ , the following conditions are imposed:

$$\begin{cases} \sigma_{el}(\mathbf{d})\mathbf{n}_{el} - \sum_{k \in J} \alpha_k p_k \mathbf{n}_{el} + \tau_f(\mathbf{u})\mathbf{n}_f - p\mathbf{n}_f = \mathbf{0}, & \text{on } \Sigma \times (0, T], & (1a) \\ p_E = p - \tau_f(\mathbf{u})\mathbf{n}_f \cdot \mathbf{n}_f, & \text{on } \Sigma \times (0, T], & (1b) \\ \frac{1}{\mu_j} k_j \nabla p_j \cdot \mathbf{n}_{el} = 0, & \text{on } \Sigma \times (0, T], \quad \forall j \in J \setminus \{E\}, & (1c) \\ \mathbf{u} \cdot \mathbf{n}_f + \left(\partial_t \mathbf{d} - \frac{1}{\mu_E} k_E \nabla p_E \right) \cdot \mathbf{n}_{el} = 0, & \text{on } \Sigma \times (0, T], & (1d) \\ (\tau_f(\mathbf{u})\mathbf{n}_f - p\mathbf{n}_f)_\tau = -\frac{\gamma \mu_f}{\sqrt{k_E}} (\mathbf{u} - \partial_t \mathbf{d})_\tau & \text{on } \Sigma \times (0, T], & (1e) \end{cases}$$

where $(\mathbf{v})_\tau = \mathbf{v} - (\mathbf{v} \cdot \mathbf{n}_f)\mathbf{n}_f$ denotes the tangential component of a vector $\mathbf{v} \in \mathbb{R}^d$ along Σ . Total stress balance is expressed by condition (1a), and the normal stress of the fluid at the pores is balanced only by the pressure of compartment E (see (1b)). Along the tangential direction, the shear stress is assumed to be proportional to the tangential velocity jump between the fluid and the poroelastic medium (see (1e)): this is the Beavers-Joseph-Saffman (BJS) condition, already adopted in the literature to model CSF perfusion interfaces [35, 6]. Notice that, although the condition is written in terms of the total stress in (1e), pressure does not actually play a role in the balance, since $(\mathbf{n}_f)_\tau = \mathbf{0}$.

In terms of boundary conditions on $\partial\Omega = (\partial\Omega_{el} \cup \partial\Omega_f) \setminus \Sigma$, we consider a portion $\Gamma_{out} \subset (\partial\Omega_f \setminus \Sigma)$ of the fluid domain boundary as an outlet and the remaining part $\Gamma_w = \partial\Omega_f \setminus (\Sigma \cup \Gamma_{out})$ as a solid wall, and also the poroelastic domain boundary $\partial\Omega_{el} \setminus \Sigma$ is partitioned into a Dirichlet and a Neumann boundary, denoted by Γ_D and Γ_N , respectively

(see Fig. 1). Denoting by $T > 0$ the final observation time, the coupled fluid-poroelastic system reads as follows:

$$\begin{cases}
\rho_{\text{el}} \partial_{tt}^2 \mathbf{d} - \nabla \cdot \sigma_{\text{el}}(\mathbf{d}) + \sum_{k \in J} \alpha_k \nabla p_k = \mathbf{f}_{\text{el}}, & \text{in } \Omega_{\text{el}} \times (0, T], & (2a) \\
c_j \partial_t p_j + \nabla \cdot \left(\alpha_j \partial_t \mathbf{d} - \frac{1}{\mu_j} k_j \nabla p_j \right) \\
+ \sum_{k \in J} \beta_{jk} (p_j - p_k) + \beta_j^e p_j = g_j, & \text{in } \Omega_{\text{el}} \times (0, T], \quad \forall j \in J, & (2b) \\
\rho_f \partial_t \mathbf{u} + \rho_f (\mathbf{u} \cdot \nabla) \mathbf{u} - \nabla \cdot \tau_f(\mathbf{u}) + \nabla p = \mathbf{f}_f, & \text{in } \Omega_f \times (0, T], & (2c) \\
\nabla \cdot \mathbf{u} = 0, & \text{in } \Omega_f \times (0, T], & (2d) \\
\left(\mathbf{d}(0), \partial_t \mathbf{d}(0) \right) = \left(\mathbf{d}_0, \dot{\mathbf{d}}_0 \right), \quad p_j(0) = p_{j0}, & \text{in } \Omega_{\text{el}}, \quad \forall j \in J, & (2e) \\
\mathbf{u}(0) = \mathbf{u}_0 & \text{in } \Omega_f, & (2f) \\
\mathbf{d} = \mathbf{0}, \quad p_j = 0, & \text{on } \Gamma_D \times (0, T], \quad \forall j \in J, & (2g) \\
\sigma_{\text{el}}(\mathbf{d}) \mathbf{n} - \sum_{j \in J} \alpha_j p_j \mathbf{n} = \mathbf{0}, \quad \frac{1}{\mu_j} k_j \nabla p_j \cdot \mathbf{n}_{\text{el}} = 0, & \text{on } \Gamma_N \times (0, T], \quad \forall j \in J, & (2h) \\
\mathbf{u} = \mathbf{0}, & \text{on } \Gamma_w \times (0, T], & (2i) \\
(\tau_f(\mathbf{u}) - pI) \mathbf{n}_f = -\bar{p}^{\text{out}} \mathbf{n}_f, & \text{on } \Gamma_{\text{out}} \times (0, T], & (2j) \\
\text{and interface conditions (1),} & \text{on } \Sigma \times (0, T], & (2k)
\end{cases}$$

with suitable definition of the source terms $\mathbf{f}_{\text{el}} : \Omega_{\text{el}} \times (0, T] \rightarrow \mathbb{R}^d$, $g_j : \Omega_{\text{el}} \times (0, T] \rightarrow \mathbb{R}$, $\mathbf{f}_f : \Omega_f \times (0, T] \rightarrow \mathbb{R}^d$, of the boundary data $\bar{p}^{\text{out}} : \Gamma_{\text{out}} \times (0, T] \rightarrow \mathbb{R}$ representing the external normal stress at the outlet, and of the initial conditions $\mathbf{d}_0 : \Omega_{\text{el}} \rightarrow \mathbb{R}^d$, $\dot{\mathbf{d}}_0 : \Omega_{\text{el}} \rightarrow \mathbb{R}^d$, $\mathbf{u}_0 : \Omega_f \rightarrow \mathbb{R}^d$, $p_{j0} : \Omega_{\text{el}} \rightarrow \mathbb{R}$, $j \in J$. Throughout the paper, the data are assumed to be sufficiently regular.

Remark 1 (Application to brain fluid-poromechanics) *The mathematical system (1)-(2) considered here can be used to model fluid-poromechanics interaction in the brain [11, 6, 33], with the fluid domain corresponding to the brain ventricles filled with CSF and the cerebral tissue being the solid matrix perfused by blood and extracellular CSF. In the fluid compartments $J = \{A, C, V, E\}$, A, C, V can represent the arterial, capillary, and venous blood networks, while the extracellular CSF ($E \in J$) is the only compartment exchanging mass with the three-dimensional CSF (cf. (1c)-(1d)), due to the blood-brain barrier. Their numerical experiments of that will be presented in Sections 7 and 8 address this application.*

The solution variables belong to the following functional spaces:

$$\mathcal{D} = H^2(0, T; \mathbf{W}), \quad \mathcal{S} = H^1(0, T; [Q_J]^{N_J}), \quad \mathcal{V} = H^1(0, T; \mathbf{V}), \quad \mathcal{Q} = L^2(0, T; Q),$$

where the notation $L^2(0, T; H)$, $H^1(0, T; H)$ denotes the time-dependent Bochner spaces associated to a Sobolev space H , and

$$\mathbf{W} = \{\mathbf{w} \in [H^1(\Omega_{\text{el}})]^d : \mathbf{w} = 0 \text{ on } \Gamma_D\}, \quad \mathbf{V} = \{\mathbf{v} \in [H^1(\Omega_f)]^d : \mathbf{v} = 0 \text{ on } \Gamma_w\},$$

$$Q_J = \{q \in H^1(\Omega_{\text{el}}) : q = 0 \text{ on } \Gamma_D\}, \quad Q = L^2(\Omega_f),$$

where $H^1(\Omega)$ denotes the classical Sobolev space of order 1 over $L^2(\Omega)$.

The weak formulation of problem (2) reads as follows:

Find $(\mathbf{d}, \{p_j\}_{j \in J}, \mathbf{u}, p) \in \mathcal{D} \times \mathcal{P} \times \mathcal{V} \times \mathcal{Q}$ such that, for all $t \in (0, T]$,

$$\begin{aligned}
& (\rho_{\text{el}} \partial_{tt}^2 \mathbf{d}, \mathbf{w})_{\Omega_{\text{el}}} + a_{\text{el}}(\mathbf{d}, \mathbf{w}) + \sum_{j \in J} b_j(p_j, \mathbf{w}) - F_{\text{el}}(\mathbf{w}) \\
& + \sum_{j \in J} \left[(c_j \partial_t p_j, q_j)_{\Omega_{\text{el}}} + a_j(p_j, q_j) + C_j(\{p_k\}_{k \in J}, q_j) - b_j(q_j, \partial_t \mathbf{d}) - F_j(q_j) \right] \\
& + (\rho_f \partial_t \mathbf{u}, \mathbf{v})_{\Omega_f} + a_f(\mathbf{u}, \mathbf{v}) + N_f(\mathbf{u}, \mathbf{u}, \mathbf{v}) + b_f(p, \mathbf{v}) + b_f(q, \mathbf{u}) - F_f(\mathbf{v}) \\
& + \mathfrak{J}(p_E, \mathbf{w}, \mathbf{v}) - \mathfrak{J}(q_E, \partial_t \mathbf{d}, \mathbf{u}) + \mathfrak{G}(\mathbf{u} - \partial_t \mathbf{d}, \mathbf{v} - \mathbf{w}) = 0
\end{aligned} \tag{3}$$

for all $(\mathbf{w}, \{q_j\}_{j \in J}, \mathbf{v}, q) \in \mathcal{D} \times \mathcal{P} \times \mathcal{V} \times \mathcal{Q}$, with $\mathbf{d}(0) = \mathbf{d}_0, \partial_t \mathbf{d}(0) = \dot{\mathbf{d}}_0, \mathbf{u}(0) = \mathbf{u}_0, p_j(0) = p_{j0} \forall j \in J$. In (3), we denoted by $(\cdot, \cdot)_{\Omega}$ the L^2 -product over Ω and we employed the following forms and functionals, where j ranges in J :

$$\begin{aligned}
a_{\text{el}} : \mathbf{W} \times \mathbf{W} &\rightarrow \mathbb{R}, & a_{\text{el}}(\mathbf{d}, \mathbf{w}) &= (\sigma_{\text{el}}(\mathbf{d}), \varepsilon(\mathbf{w}))_{\Omega_{\text{el}}}, \\
a_j : Q_J \times Q_J &\rightarrow \mathbb{R}, & a_j(p_j, q_j) &= \left(\frac{1}{\mu_j} k_j \nabla p_j, \nabla q_j \right)_{\Omega_{\text{el}}}, \\
C_j : [Q_J]^{N_J} \times Q_J &\rightarrow \mathbb{R}, & C_j(\{p_k\}_{k \in J}, q_j) &= \sum_{k \in J} (\beta_{kj} (p_j - p_k), q_j)_{\Omega_{\text{el}}} + (\beta_j^e p_j, q_j)_{\Omega_{\text{el}}}, \\
a_f : \mathbf{V} \times \mathbf{V} &\rightarrow \mathbb{R}, & a_f(\mathbf{u}, \mathbf{v}) &= (\tau_f(\mathbf{u}), \varepsilon(\mathbf{v}))_{\Omega_f}, \\
N_f : \mathbf{V} \times \mathbf{V} \times \mathbf{V} &\rightarrow \mathbb{R}, & N_f(\mathbf{u}', \mathbf{u}, \mathbf{v}) &= \left(\rho_f (\mathbf{u}' \cdot \nabla) \mathbf{u} + \frac{\rho_f}{2} (\nabla \cdot \mathbf{u}') \mathbf{u}, \mathbf{v} \right)_{\Omega_f}, \\
b_j : Q_J \times \mathbf{W} &\rightarrow \mathbb{R}, & b_j(q_j, \mathbf{w}) &= -(\alpha_j q_j, \text{div} \mathbf{w})_{\Omega_{\text{el}}}, \\
b_f : Q \times \mathbf{V} &\rightarrow \mathbb{R}, & b_f(q, \mathbf{v}) &= -(q, \text{div} \mathbf{v})_{\Omega_f}, \\
F_{\text{el}} : \mathbf{W} &\rightarrow \mathbb{R}, & F_{\text{el}}(\mathbf{w}) &= (\mathbf{f}_{\text{el}}, \mathbf{w})_{\Omega_{\text{el}}}, \\
F_j : Q_J &\rightarrow \mathbb{R}, & F_j(q_j) &= (g_j, q_j)_{\Omega_{\text{el}}}, \\
F_f : \mathbf{V} &\rightarrow \mathbb{R}, & F_f(\mathbf{v}) &= (\mathbf{f}_f, \mathbf{v})_{\Omega_f}, \\
\mathfrak{J} : Q_J \times \mathbf{W} \times \mathbf{V} &\rightarrow \mathbb{R}, & \mathfrak{J}(p_E, \mathbf{w}, \mathbf{v}) &= \int_{\Sigma} p_E (\mathbf{w} \cdot \mathbf{n}_{\text{el}} + \mathbf{v} \cdot \mathbf{n}_f) d\Sigma, \\
\mathfrak{G} : (\mathbf{V} \oplus \mathbf{W}) \times (\mathbf{V} \oplus \mathbf{W}) &\rightarrow \mathbb{R}, & \mathfrak{G}(\mathbf{z}_1, \mathbf{z}_2) &= \int_{\Sigma} \frac{\gamma \mu_f}{\sqrt{k_E}} (\mathbf{z}_1)_{\tau} \cdot (\mathbf{z}_2)_{\tau} d\Sigma.
\end{aligned} \tag{4}$$

We point out that, differently from the models studied in [11, 33], here we consider the following additional terms: the trilinear form N_f and the interface form \mathfrak{G} , discussed in the following remarks.

Remark 2 (Skew-symmetry of the advection form N_f) *In the trilinear form N_f , we have introduced the additional term $(\frac{\rho_f}{2} (\nabla \cdot \mathbf{u}'), \mathbf{v})_{\Omega_f}$, classically employed for Navier-Stokes problems [36]. This term vanishes if \mathbf{u}' is the fluid velocity \mathbf{u} of (2), but it ensures that that N_f is skew-symmetric w.r.t. exchanging the second and third argument also if \mathbf{u}' is such that $\nabla \cdot \mathbf{u}' \neq 0$, as it may occur after the discretization of the equations.*

Remark 3 (Derivation of the interface forms \mathfrak{J} and \mathfrak{G}) *The interface forms \mathfrak{J} and \mathfrak{G} introduced above naturally arise during the derivation of the weak form of problem (2). We test (2a)-(2b) against functions $\mathbf{w} \in \mathbf{W}$ and $q_j \in Q_J$, with $j \in J$, over Ω_{el} , and (2c) against $\mathbf{v} \in \mathbf{V}$ over Ω_f . Then, integrating by parts and summing all the contributions yield the following boundary terms on the interface:*

$$\int_{\Sigma} \left[(pI - \tau_f(\mathbf{u})) : \mathbf{v} \otimes \mathbf{n}_f + \left(\sum_{k \in J} \alpha_k p_k I - \sigma_{\text{el}}(\mathbf{d}) \right) : \mathbf{w} \otimes \mathbf{n}_{\text{el}} - \sum_{j \in J} \frac{1}{\mu_j} k_j \nabla p_j \cdot q_j \mathbf{n}_{\text{el}} \right] d\Sigma. \tag{5}$$

Using the interface conditions (1a),(1c) and then (1b),(1d),(1e), we can rewrite (5) as follows:

$$\begin{aligned}
& \int_{\Sigma} \left[(pI - \tau_f(\mathbf{u})) : (\mathbf{v} \otimes \mathbf{n}_f + \mathbf{w} \otimes \mathbf{n}_{el}) - \frac{1}{\mu_E} k_E \nabla p_E \cdot q_E \mathbf{n}_{el} \right] d\Sigma \\
&= \int_{\Sigma} \left[p_E (\mathbf{v} \cdot \mathbf{n}_f + \mathbf{w} \cdot \mathbf{n}_{el}) + \frac{\gamma \mu_f}{\sqrt{k_E}} (\mathbf{u} - \partial_t \mathbf{d})_{\tau} \cdot (\mathbf{v} - \mathbf{w})_{\tau} - q_E (\mathbf{u} \cdot \mathbf{n}_f + \partial_t \mathbf{d} \cdot \mathbf{n}_{el}) \right] d\Sigma \\
&= \mathfrak{J}(p_E, \mathbf{w}, \mathbf{v}) + \mathfrak{G}(\mathbf{u} - \partial_t \mathbf{d}, \mathbf{v} - \mathbf{w}) - \mathfrak{J}(q_E, \partial_t \mathbf{d}, \mathbf{u}),
\end{aligned} \tag{6}$$

where we also used that $\mathbf{a} \otimes \mathbf{b} : \mathbf{I} = \mathbf{a} \cdot \mathbf{b}$ for any $\mathbf{a}, \mathbf{b} \in \mathbb{R}^d$, and that $\mathbf{n}_f = -\mathbf{n}_{el}$ on Σ .

3 Polytopal discontinuous Galerkin semi-discrete formulation

In this section, we introduce the space discretization of problem (3) by a discontinuous Finite Element method on polytopal grids.

Let $\mathcal{T}_{h,el}, \mathcal{T}_{h,f}$ be polytopal meshes discretizing the domains Ω_{el}, Ω_f , respectively. We define the *faces* of an element $K \in \mathcal{T}_{h,el} \cup \mathcal{T}_{h,f}$ as the $(d-1)$ -dimensional entities constituting the intersection of ∂K with either the boundary of a neighboring element or the domain boundary $\partial\Omega$. For $d=2$ all faces are straight line segments, while for $d=3$ they are generic polygons, in principle: we assume that each of these polygons can be further decomposed into triangles, and we define as *face* each of these triangles. We collect all faces in each physical domain into \mathcal{F}_{el} and \mathcal{F}_f , and we partition these sets into internal faces $\mathcal{F}_{el}^1, \mathcal{F}_{el}^1$, Dirichlet/Neumann faces $\mathcal{F}_{el}^D / \mathcal{F}_{el}^N \subset \partial\Omega_{el} \setminus \Sigma, \mathcal{F}_f^D / \mathcal{F}_f^N \subset \partial\Omega_f \setminus \Sigma$ (as portions of the poroelastic and the fluid domain boundaries, respectively), and interface faces $\mathcal{F}^{\Sigma} \subset \Sigma$. We assume that the polytopal grids $\mathcal{T}_{h,el}, \mathcal{T}_{h,f}$ are geometrically conforming with Σ , but possibly not mesh-conforming.

Over each mesh $\mathcal{T}_{h,\star}, \star \in \{el, f\}$, we introduce the broken Sobolev spaces of order s , namely $H^s(\mathcal{T}_{h,\star}) = \{q \in L^2(\Omega_{\star}) : q|_K \in H^s(K) \quad \forall K \in \mathcal{T}_{h,\star}\}$. Moreover, we define the following piecewise polynomial spaces for a given integer $m \geq 1$:

$$\begin{aligned}
X_h^{DG}(\mathcal{T}_{h,\star}) &= \{\phi \in L^2(\Omega_{\star}) : \phi|_K \in \mathbb{P}^m(K) \quad \forall K \in \mathcal{T}_{h,\star}\}, \quad \star \in \{el, f\} \\
Q_{J,h}^{DG} &= X_h^{DG}(\mathcal{T}_{h,el}), \quad Q_h^{DG} = X_h^{DG}(\mathcal{T}_{h,f}), \quad \mathbf{W}_h^{DG} = [X_h^{DG}(\mathcal{T}_{h,el})]^d, \quad \mathbf{V}_h^{DG} = [X_h^{DG}(\mathcal{T}_{h,f})]^d.
\end{aligned}$$

To introduce the PolyDG discretization of (3), we define the symmetric outer product $\mathbf{v} \odot \mathbf{n} = \frac{1}{2}(\mathbf{v} \otimes \mathbf{n} + \mathbf{n} \otimes \mathbf{v})$ and, for regular enough scalar-, vector- and tensor-valued functions q, \mathbf{v}, τ , we define the following average and jump operators.

- On each internal face $F \in \mathcal{F}^I = \mathcal{F}_{el}^I \cup \mathcal{F}_f^I$ we set:

$$\begin{aligned}
\{\!\{q\}\!\} &= \frac{1}{2}(q^+ + q^-), & \{\!\{\mathbf{v}\}\!\} &= \frac{1}{2}(\mathbf{v}^+ + \mathbf{v}^-), & \{\!\{\tau\}\!\} &= \frac{1}{2}(\tau^+ + \tau^-), \\
\llbracket q \rrbracket &= q^+ \mathbf{n}^+ + q^- \mathbf{n}^-, & \llbracket \mathbf{v} \rrbracket &= \mathbf{v}^+ \odot \mathbf{n}^+ + \mathbf{v}^- \odot \mathbf{n}^-, & \llbracket \tau \rrbracket &= \tau^+ \mathbf{n}^+ + \tau^- \mathbf{n}^-.
\end{aligned}$$

where $\mathbf{n}^+, \mathbf{n}^-$ are defined as in Fig. 2 - left.

- On a Dirichlet face $F \in \mathcal{F}_{el}^D \cup \mathcal{F}_f^D$ we set:

$$\begin{aligned}
\{\!\{q\}\!\} &= q, & \{\!\{\mathbf{v}\}\!\} &= \mathbf{v}, & \{\!\{\tau\}\!\} &= \tau, \\
\llbracket q \rrbracket &= q\mathbf{n}, & \llbracket \mathbf{v} \rrbracket &= \mathbf{v} \odot \mathbf{n}, & \llbracket \tau \rrbracket &= \tau\mathbf{n},
\end{aligned}$$

where \mathbf{n} is the unit normal vector pointing outward to the element K to which the face F belongs.

- On a face $F \in \mathcal{F}^{\Sigma}$ shared by two elements $K_{el} \in \mathcal{T}_{h,el}$ and $K_f \in \mathcal{T}_{h,f}$ we set:

$$\begin{aligned}
\{\!\{q\}\!\} &= q|_{K_{el}}, & \{\!\{\tau\}\!\} &= \tau|_{K_{el}}, \\
\llbracket \mathbf{w}, \mathbf{v} \rrbracket &= \mathbf{w}|_{K_{el}} \odot \mathbf{n}_{el} + \mathbf{v}|_{K_f} \odot \mathbf{n}_f, & \llbracket \mathbf{w}, \mathbf{v} \rrbracket_{\tau} &= (\mathbf{v}|_{K_f})_{\tau} - (\mathbf{w}|_{K_{el}})_{\tau},
\end{aligned}$$

where $\mathbf{n}_{el}, \mathbf{n}_f$ are defined as in Fig. 2 - right. Notice that the definitions of the interface jump operators account for the different physics defined on each side of the interface.

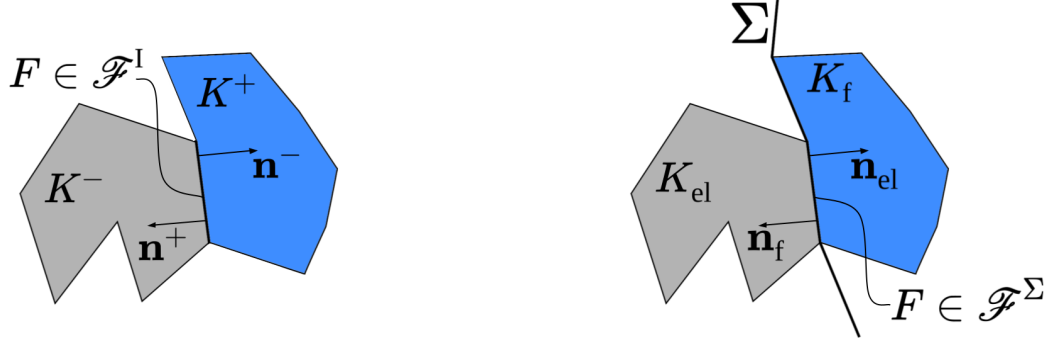


Figure 2: Polygonal elements sharing an internal face (left) or a face on the interface Σ (right).

Based on the spaces and the trace operators defined above, the semidiscrete formulation of problem (3) reads as follows:

For any $t \in (0, T]$, find $(\mathbf{d}_h, \{p_{j,h}\}_{j \in J}, \mathbf{u}_h, p_h) \in \mathbf{W}_h^{\text{DG}} \times [Q_{J,h}^{\text{DG}}]^{N_J} \times \mathbf{V}_h^{\text{DG}} \times Q_h^{\text{DG}}$ such that

$$\begin{aligned}
& (\rho_{el} \partial_{tt}^2 \mathbf{d}_h, \mathbf{w}_h)_{\Omega_{el}} + \mathcal{L}_{el}(\mathbf{d}_h, \{p_{k,h}\}_{k \in J}; \mathbf{w}_h) - \mathcal{F}_{el}(\mathbf{w}_h) \\
& + \sum_{j \in J} [(c_j \partial_t p_{j,h}, q_{j,h})_{\Omega_{el}} + \mathcal{L}_j(\{p_{k,h}\}_{k \in J}, \partial_t \mathbf{d}_h; q_{j,h}) - \mathcal{F}_j(q_{j,h})] \\
& + (\rho_f \partial_t \mathbf{u}_h, \mathbf{v}_h)_{\Omega_f} + \mathcal{L}_f(\mathbf{u}_h, p_h; \mathbf{v}_h, q_h) - \mathcal{F}_f(\mathbf{v}_h) \\
& + \mathcal{J}(p_{E,h}, \mathbf{w}_h, \mathbf{v}_h) - \mathcal{J}(q_{E,h}, \partial_t \mathbf{d}_h, \mathbf{u}_h) + \mathcal{G}(\mathbf{u}_h - \partial_t \mathbf{d}_h, \mathbf{v}_h - \mathbf{w}_h) = 0 \\
& \forall \mathbf{w}_h \in \mathbf{W}_h^{\text{DG}}, \mathbf{v}_h \in \mathbf{V}_h^{\text{DG}}, q_h \in Q_h^{\text{DG}}, q_{j,h} \in Q_{J,h}^{\text{DG}},
\end{aligned} \tag{7}$$

with initial conditions defined in terms of the projections $\mathbf{d}_h(0), \dot{\mathbf{d}}_h(0), \{p_{j,h}(0)\}_{j \in J}, \mathbf{u}_h(0)$ of the initial data introduced in (2) onto the corresponding DG spaces. The forms and functionals appearing in (7) are the PolyDG version of those defined in (4) and their complete definitions can be found in Appendix A. Here we just report the definition of the interface terms, to show the role of the interface jump operators:

$$\begin{aligned}
\mathcal{J}(p_E, \mathbf{w}, \mathbf{v}) &= \sum_{F \in \mathcal{F}^\Sigma} \int_F (\{p_E I\}: [\mathbf{w}, \mathbf{v}]), \\
\mathcal{G}(\mathbf{v}_1 - \mathbf{w}_1, \mathbf{v}_2 - \mathbf{w}_2) &= \sum_{F \in \mathcal{F}^\Sigma} \int_F \frac{\gamma \mu_f}{\sqrt{k_E}} [\mathbf{w}_1, \mathbf{v}_1]_\tau \cdot [\mathbf{w}_2, \mathbf{v}_2]_\tau.
\end{aligned}$$

Moreover, we point out that the definitions of $\mathcal{L}_{el}, \mathcal{L}_f, \mathcal{L}_j, j \in J$, include stabilization terms with parameters that depend on the mesh element size (see Appendix A), that will be useful in the theoretical analysis of Section 4. However, these stabilization terms are defined only on internal faces and do not contribute to the interface terms.

4 Stability and error analysis of the semidiscrete Stokes-MPE problem

In this section, we analyze the semidiscrete problem corresponding to a choice of the Stokes equations to model the CSF flow in Ω_f , namely we neglect the nonlinear advection term in the form \mathcal{L}_f of (7) (see form \mathcal{N}_f in (17c)). The following analysis holds for a generic set J made of $N_J \in \mathbb{N}_0$ fluid compartments of the poroelastic model. For the sake of simplicity, we make the following assumptions.

Assumption 1

- all the physical parameters of the model (cf. Table 1) are piecewise constant according to the aforementioned decomposition;
- the polytopal mesh $\mathcal{T}_h = \mathcal{T}_{h,\text{el}} \cup \mathcal{T}_{h,\text{f}}$ fulfills the regularity assumptions of the PolyDG framework, namely that \mathcal{T}_h is h -uniformly polytopic-regular, a local bounded variation property holds, and there exists a suitable shape-regular simplicial covering of \mathcal{T}_h [37, 38].

In all the inequalities appearing hereafter, the dependency on the model parameters and the finite element degree m will be neglected: by $x \lesssim y$ we will indicate that $\exists C > 0 : x \leq Cy$, with C independent of the space discretization parameters.

Following [33, 11, 15], we define the following broken norms:

$$\|\mathbf{d}\|_{\text{DG},\text{D}}^2 = \|\mathbb{C}_{\text{el}}^{1/2}[\varepsilon_h(\mathbf{d})]\|_{L^2(\mathcal{T}_{h,\text{el}})}^2 + \|\sqrt{\gamma}[\mathbf{d}]\|_{\mathcal{F}_{\text{el},h}^{\text{I}} \cup \mathcal{F}_{\text{el},h}^{\text{D}}}^2 \quad \forall \mathbf{d} \in \mathbf{H}^1(\mathcal{T}_h), \quad (8a)$$

$$\|p\|_{\text{DG},\text{P}_j}^2 = \|\mu_j^{-1/2} k_j^{1/2} \nabla_h p\|_{L^2(\mathcal{T}_{h,\text{el}})}^2 + \|\sqrt{\zeta_j}[p]\|_{\mathcal{F}_{\text{el},h}^{\text{I}} \cup \mathcal{F}_{\text{el},h}^{\text{D}_j}}^2 \quad \forall p \in H^1(\mathcal{T}_h), \quad (8b)$$

$$\|\mathbf{u}\|_{\text{DG},\text{U}}^2 = \|\sqrt{2\mu} \varepsilon_h(\mathbf{u})\|_{L^2(\mathcal{T}_{h,\text{f}})}^2 + \|\sqrt{\gamma_v}[\mathbf{u}]\|_{\mathcal{F}_{\text{f},h}^{\text{I}}}^2 \quad \forall \mathbf{u} \in \mathbf{H}^1(\mathcal{T}_h), \quad (8c)$$

$$\|q\|_{\text{DG},\text{P}_f}^2 = \|q\|_{L^2(\Omega_f)}^2 + \|\sqrt{\gamma_p}[q]\|_{\mathcal{F}_{\text{f},h}^{\text{I}} \cup \mathcal{F}_{\text{f},h}^{\text{D}}}^2 \quad \forall q \in H^1(\mathcal{T}_h), \quad (8d)$$

and we introduce the following energy norms at time $t \in (0, T]$, based on those broken norms but also depending on the tangential velocity of the fluid and of the poroelastic structure along the interface Σ :

$$\|(\mathbf{d}, \{p_j\}_{j \in J}, \mathbf{u}, p)\|_{\text{EN},t} = [\|(\mathbf{d}, \{p_j\}_{j \in J})\|_{\text{el},t}^2 + \|(\mathbf{u}, p)\|_{\text{f},t}^2 + |(\mathbf{u}, \partial_t \mathbf{d})|_{\tau,t}^2]^{1/2}, \quad (9)$$

where

$$\begin{aligned} \|(\mathbf{d}, \{p_j\}_{j \in J})\|_{\text{el},t} &= \left[\|\sqrt{\rho_{\text{el}}} \partial_t \mathbf{d}(t)\|_{\Omega_{\text{el}}}^2 + \|\mathbf{d}(t)\|_{\text{DG},\text{D}}^2 \right. \\ &\quad \left. + \sum_{j \in J} \left(\|\sqrt{c_j} p_j(t)\|_{\Omega_{\text{el}}}^2 + \int_0^t \left(\|p_j(s)\|_{\text{DG},\text{P}_j}^2 + \|\sqrt{\beta_j^e} p_j(s)\|_{\Omega_{\text{el}}}^2 \right) ds \right) \right]^{1/2}, \\ \|(\mathbf{u}, p)\|_{\text{f},t} &= \left[\|\sqrt{\rho_f} \mathbf{u}(t)\|_{\Omega_f}^2 + \int_0^t \left(\|\mathbf{u}(s)\|_{\text{DG},\text{U}}^2 + \|p(s)\|_{\text{DG},\text{P}_f}^2 \right) ds \right]^{1/2}, \\ |(\mathbf{u}, \partial_t \mathbf{d})|_{\tau,t} &= \left[\int_0^t \mathcal{G}(\mathbf{u}(s) - \partial_t \mathbf{d}(s), \mathbf{u}(s) - \partial_t \mathbf{d}(s)) ds \right]^{1/2}. \end{aligned}$$

Based on these norms, we can prove the following stability result:

Theorem 1 (Stability estimate) *Under Assumption 1 and assuming that sufficiently large values are chosen for the penalty constants (cf. (20)), the solution $(\mathbf{d}_h, \{p_{j,h}\}_{j \in J}, \mathbf{u}_h, p_h)$ of the semidiscrete problem (7) fulfills the following inequality for each time $t \in (0, T]$:*

$$\begin{aligned} \|(\mathbf{d}_h, \{p_{j,h}\}_{j \in J}, \mathbf{u}_h, p_h)\|_{\text{EN},t} &\lesssim \|(\mathbf{d}_h, \{p_{j,h}\}_{j \in J}, \mathbf{u}_h, 0)\|_{\text{EN},0} \\ &\quad + \int_0^t \left(\frac{1}{\sqrt{\rho_{\text{el}}}} \|\mathbf{f}_{\text{el}}\|_{\Omega_{\text{el}}} + \sum_{j \in J} \frac{1}{\sqrt{c_j}} \|g_j\|_{\Omega_{\text{el}}} + \frac{1}{\sqrt{\rho_f}} \|\mathbf{f}_f\|_{\Omega_f} \right) ds, \end{aligned} \quad (10)$$

where the first term depends on the initial conditions (2e)-(2f):

$$\|(\mathbf{d}_h, \{p_{j,h}\}_{j \in J}, \mathbf{u}_h, 0)\|_{\text{EN},0} = \left[\|\sqrt{\rho_{\text{el}}} \mathbf{d}_h^0\|_{\Omega_{\text{el}}}^2 + \|\mathbf{d}_h^0\|_{\text{DG},\text{D}}^2 + \sum_{j \in J} \|\sqrt{c_j} p_{j,h}^0\|_{\Omega_{\text{el}}}^2 + \|\sqrt{\rho_f} \mathbf{u}_h^0\|_{\Omega_f}^2 \right]^{1/2}.$$

Proof. Choosing the test functions $\mathbf{w}_h = \partial_t \mathbf{d}_h(t)$, $\mathbf{v}_h = \mathbf{u}_h(t)$, $q_h = p_h(t)$, $q_{j,h} = p_{j,h}(t) \forall j \in J$ in the semidiscrete problem (7) and following the arguments of [33, Theorem 4.1], we obtain the following inequality:

$$\|(\mathbf{d}, \{p_j\}_{j \in J})\|_{\text{el},t}^2 + \|(\mathbf{u}, p)\|_{\text{f},t}^2 + \int_0^t \mathcal{G}(\mathbf{u}_h(s) - \partial_t \mathbf{d}_h(s), \mathbf{u}_h(s) - \partial_t \mathbf{d}_h(s)) ds \leq \text{RHS},$$

where RHS denotes the right-hand side of (10). Observing that the term with the form \mathcal{G} coincides with the definition of $\|(\mathbf{u}_h, \partial_t \mathbf{d}_h)\|_{\tau,t}^2$ concludes the proof.

Remark 4 We point out that the semi-discrete problem (7) is stable in the Navier-Stokes case, too, since the advection form N_{f} is skew-symmetric and thus cancels out in the proof of Theorem 1.

To derive an a-priori estimate for the space discretization error of the proposed PolyDG method, we rely on the following additional norms for non-discrete functions:

$$\begin{aligned} \|\mathbf{w}\|_{\text{D}}^2 &= \|\mathbf{w}\|_{\text{DG,D}}^2 + \|\eta^{-1/2} \{\{\sigma_{\text{el}}(\mathbf{w})\}\}\|_{\mathcal{F}_{\text{el},h}^1 \cup \mathcal{F}_{\text{el},h}^{\text{D}}}^2 & \forall \mathbf{w} \in [H^2(\mathcal{T}_{h,\text{el}})]^d, \\ \|q_j\|_{\text{P}_j}^2 &= \|q_j\|_{\text{DG,P}_j}^2 + \|\zeta^{-1/2} \{\{\frac{1}{\mu_j} k_j \nabla_h q_j\}\}\|_{\mathcal{F}_{\text{el},h}^1 \cup \mathcal{F}_{\text{el},h}^{\text{D}_j}}^2 & \forall q_j \in H^2(\mathcal{T}_{h,\text{el}}), \quad \forall j \in J, \\ \|\mathbf{v}\|_{\text{U}}^2 &= \|\mathbf{v}\|_{\text{DG,U}}^2 + \|\gamma_v^{-1/2} \{\{\tau_{\text{f}}(\mathbf{v})\}\}\|_{\mathcal{F}_{\text{f},h}^1 \cup \mathcal{F}_{\text{f},h}^{\text{D}}}^2 & \forall \mathbf{v} \in [H^2(\mathcal{T}_{h,\text{f}})]^d, \\ \|q\|_{\text{P}_f}^2 &= \|q\|_{\text{DG,P}_f}^2 + \|\gamma_p^{-1/2} \{\{q\}\}\|_{\mathcal{F}_{\text{f},h}^1}^2 & \forall q \in H^1(\mathcal{T}_{h,\text{f}}), \\ \|(\mathbf{w}, \{q_j\}_{j \in J}, \mathbf{v}, p)\|^2 &= \|\mathbf{w}\|_{\text{D}}^2 + \sum_{j \in J} \|q_j\|_{\text{P}_j}^2 + \|\mathbf{v}\|_{\text{U}}^2 + \|q\|_{\text{P}_f}^2. \end{aligned}$$

Moreover, we denote by $\mathcal{E}_K : H^s(\Omega) \rightarrow H^s(\mathbb{R}^d)$ the Stein extension operator from a Lipschitz domain Ω defined in [39], for which optimal interpolation results can be proven w.r.t. the norms defined above (cf. Appendix B). Combining the results above, we can prove the following optimal convergence estimate:

Theorem 2 (A priori error estimate) *Let us assume that Assumption 1 holds and that the penalty parameters included in the discrete problem's formulation are sufficiently large (see (20)). If the solution of problem (3) is sufficiently regular, the following estimate holds for each $t \in (0, T]$:*

$$\begin{aligned} & \|(\mathbf{e}^{\mathbf{d}}, \{e^{p_j}\}_{j \in J}, \mathbf{e}^{\mathbf{u}}, e^p)\|_{\text{EN},t}^2 \\ & \lesssim \sum_{K \in \mathcal{T}_{h,\text{el}}} h_K^{2m} \left\{ \|\mathcal{E}_K \mathbf{d}(t)\|_{[H^{m+1}(\widehat{K})]^d}^2 + \sum_{k \in J} \|\mathcal{E}_K p_k(t)\|_{H^{m+1}(\widehat{K})}^2 \right. \\ & \quad + \int_0^t \left[\|\mathcal{E}_K \partial_t \mathbf{d}(s)\|_{[H^{m+1}(\widehat{K})]^d}^2 + \|\mathcal{E}_K \partial_{tt}^2 \mathbf{d}(s)\|_{[H^{m+1}(\widehat{K})]^d}^2 \right] ds \\ & \quad \left. + \int_0^t \sum_{k \in J} \left(\|\mathcal{E}_K p_k(s)\|_{H^{m+1}(\widehat{K})}^2 + \|\mathcal{E}_K \partial_t p_k(s)\|_{H^{m+1}(\widehat{K})}^2 \right) ds \right\} \\ & \quad + \sum_{K \in \mathcal{T}_{h,\text{f}}} h_K^{2m} \int_0^t \left[\|\mathcal{E}_K \mathbf{u}(s)\|_{[H^{m+1}(\widehat{K})]^d}^2 + \|\mathcal{E}_K \partial_t \mathbf{u}(s)\|_{[H^{m+1}(\widehat{K})]^d}^2 \right. \\ & \quad \left. + \|\mathcal{E}_K p(s)\|_{H^{m+1}(\widehat{K})}^2 \right] ds, \end{aligned} \tag{11}$$

where $\mathbf{e}^{\mathbf{d}} = \mathbf{d} - \mathbf{d}_h$, $e^{p_j} = p_j - p_{j,h} \forall j \in J$, $\mathbf{e}^{\mathbf{u}} = \mathbf{u} - \mathbf{u}_h$, $e^p = p - p_h$, and $\widehat{K} \supseteq K$, for each $K \in \mathcal{T}_h$, are shape-regular simplexes covering \mathcal{T}_h , as in Assumption 1.

Proof. Considering the continuous displacement \mathbf{d} and its semi-discrete counterpart \mathbf{d}_h , we introduce the error splitting $\mathbf{d} - \mathbf{d}_h = \mathbf{e}_I^{\mathbf{d}} - \mathbf{e}_h^{\mathbf{d}}$, with $\mathbf{e}_I^{\mathbf{d}} = \mathbf{d} - \mathbf{d}_I \in [H^{m+1}(\mathcal{T}_{h,\text{el}})]^d$ being the Stein interpolation error (cf. Lemma 1 in Appendix B) and $\mathbf{e}_h^{\mathbf{d}} = \mathbf{d}_h - \mathbf{d}_I \in \mathbf{W}_h^{\text{DG}}$ being the approximation error. Analogous definitions are introduced for $e^{p_j} \forall j \in J, \mathbf{e}^{\mathbf{u}}, e^p$. We subtract the continuous problem (3) from the semi-discrete problem (7), tested against $(\partial_t \mathbf{e}_h^{\mathbf{d}}, \{e_h^{p_j}\}_{j \in J}, \mathbf{e}_h^{\mathbf{u}}, e_h^p)$, we apply the coercivity of the bilinear forms $\mathcal{L}_{\text{el}}, \mathcal{L}_f, \mathcal{L}_{j,j} \in J$, and the continuity of these forms as well as of J (cf. [33, Lemmas 2 and 5]), and then we can follow the same steps of [33, Theorem 4.2] to arrive to the following inequality:

$$\begin{aligned} & \|(\mathbf{e}_h^{\mathbf{d}}, \{e_h^{p_j}\}_{j \in J})\|_{\text{el},t}^2 + \|(\mathbf{e}_h^{\mathbf{u}}, e_h^p)\|_{f,t}^2 + \int_0^t \mathcal{G}(\mathbf{e}_h^{\mathbf{u}}(s) - \partial_t \mathbf{e}_h^{\mathbf{d}}(s), \mathbf{e}_h^{\mathbf{u}}(s) - \partial_t \mathbf{e}_h^{\mathbf{d}}(s)) ds \\ & \lesssim \text{RHS} + \int_0^t \mathcal{G}(\mathbf{e}_I^{\mathbf{u}}(s) - \partial_t \mathbf{e}_I^{\mathbf{d}}(s), \mathbf{e}_h^{\mathbf{u}}(s) - \partial_t \mathbf{e}_h^{\mathbf{d}}(s)) ds \\ & \lesssim \text{RHS} + |(\mathbf{e}_I^{\mathbf{u}}, \partial_t \mathbf{e}_I^{\mathbf{d}})|_{\tau,t} |(\mathbf{e}_h^{\mathbf{u}}, \partial_t \mathbf{e}_h^{\mathbf{d}})|_{\tau,t}, \end{aligned} \quad (12)$$

where RHS is the right-hand side of the thesis (11). We have used the linearity of \mathcal{G} and the fact that the squared energy norm defined in this work corresponds to that of [33] plus the tangential velocity squared seminorm $|(\mathbf{e}_h^{\mathbf{u}}, \partial_t \mathbf{e}_h^{\mathbf{d}})|_{\tau,t}^2 = \int_0^t \mathcal{G}(\mathbf{e}_h^{\mathbf{u}}(s) - \partial_t \mathbf{e}_h^{\mathbf{d}}(s), \mathbf{e}_h^{\mathbf{u}}(s) - \partial_t \mathbf{e}_h^{\mathbf{d}}(s)) ds$. Now, since the seminorm $|(\mathbf{e}_I^{\mathbf{u}}, \partial_t \mathbf{e}_I^{\mathbf{d}})|_{\tau,t}$ can be controlled by the corresponding broken L^2 norm over the interface faces $F \in \mathcal{F}^\Sigma$, we can employ Stein interpolation results and obtain the following (see Appendix B):

$$\begin{aligned} & |(\mathbf{e}_I^{\mathbf{u}}, \partial_t \mathbf{e}_I^{\mathbf{d}})|_{\tau,t} \\ & \lesssim \int_0^t \left(\|\mathbf{e}_I^{\mathbf{u}}(s)\|_{\mathcal{F}^\Sigma} + \|\partial_t \mathbf{e}_I^{\mathbf{d}}(s)\|_{\mathcal{F}^\Sigma} \right) ds \\ & \lesssim \int_0^t \left(\sum_{\substack{K \in \mathcal{T}_{h,f} \\ \partial K \cap \Sigma \neq \emptyset}} h_K^{m+1/2} \|\mathcal{E}\mathbf{u}(s)\|_{H^{m+1}(\widehat{K})} + \sum_{\substack{K \in \mathcal{T}_{h,f} \\ \partial K \cap \Sigma \neq \emptyset}} h_K^{m+1/2} \|\mathcal{E}\partial_t \mathbf{d}(s)\|_{H^{m+1}(\widehat{K})} \right) ds, \end{aligned}$$

where $\widehat{K} \supseteq K$, for each $K \in \mathcal{T}_h$, are shape-regular simplexes covering \mathcal{T}_h , existing thanks to Assumption 1. Then, the application of Cauchy-Schwarz and Young inequalities on (12) concludes the proof.

Remark 5 *It is worth to point out that, in the proof of Theorem 2, the contribution of the interpolation error in the $|\cdot|_{\tau,t}$ seminorm has a convergence order that is 1/2 greater than the other terms of the energy norm. This means that the treatment of the BJS condition in the proposed numerical method does not affect convergence.*

5 Fully discrete problem and implementation

Starting from the semi-discrete problem (7), we introduce a timestep Δt and a corresponding time discretization over a uniform partition $\{t^n = n\Delta t\}_{n=0}^N$ of the interval $(0, T]$. We use Newmark's β -method to discretize the terms tested against \mathbf{w}_h in (7) (corresponding to the elastic momentum equation) and the Crank-Nicolson method for all the other terms. The nonlinear advection term is linearized by a semi-implicit approach, using a second-order extrapolation of the advecting velocity at time $t^{n+1/2}$:

$$(\mathbf{u} \cdot \nabla) \mathbf{u} \big|_{t=t^{n+1/2}} \simeq \left[\left(\frac{3}{2} \mathbf{u}^n - \frac{1}{2} \mathbf{u}^{n-1} \right) \cdot \nabla \right] \frac{\mathbf{u}^{n+1} + \mathbf{u}^n}{2}, \quad (13)$$

where the superscript n denotes the discrete variable approximating \mathbf{u} at time t^n . A similar notation is used in the following for all the other variables.

In accordance with the above discretization methods, the algebraic form of the fully discrete problem reads as follows:

$$A_1(\mathbf{U}^n, \mathbf{U}^{n-1})\mathbf{X}^{n+1} = A_2(\mathbf{U}^n, \mathbf{U}^{n-1})\mathbf{X}^n + \mathbf{F}^{n+1}, \quad n = 1, \dots, N, \quad (14)$$

where

$$\mathbf{X}^n = [\mathbf{D}^n; \mathbf{Z}^n; \mathbf{A}^n; \mathbf{P}_A^n; \dots; \mathbf{P}_E^n; \mathbf{U}^n; \mathbf{P}^n], \quad \mathbf{F}^{n+1} = [\mathbf{F}_{\text{el}}^n; \mathbf{0}; \mathbf{0}; \mathbf{F}_A^{\text{CN}}; \dots; \mathbf{F}_E^{\text{CN}}; \mathbf{F}_f^{\text{CN}}; \mathbf{0}]. \quad (15)$$

To employ Newmark's scheme, we have introduced two auxiliary vector variables $\mathbf{Z}^n, \mathbf{A}^n$ representing the first and second time derivatives of \mathbf{D}^n . The definition of the matrices $A_1(\mathbf{U}^n, \mathbf{U}^{n-1}), A_2(\mathbf{U}^n, \mathbf{U}^{n-1})$ can be obtained with slight changes from those reported in [33]. Specifically, the Navier-Stokes advection term encompasses a modification of the diagonal block corresponding to the fluid velocity \mathbf{U} , while the BJS condition yields the addition of the following matrix in the diagonal blocks corresponding to the solid and fluid velocities \mathbf{Z} and \mathbf{U} , and their mutual coupling:

$$[G_{\star, \Delta}]_{ij} = \sum_{F \in \mathcal{F}^\Sigma} \int_F \frac{\gamma \mu_{\text{f}}}{\sqrt{k_{\text{E}}}} (\varphi_{\star}^j)_{\tau} \cdot (\varphi_{\Delta}^i)_{\tau}, \quad \star \in \{\text{el}, \text{f}\}, \quad \Delta \in \{\text{el}, \text{f}\},$$

where the integrand is expressed in terms of the basis functions of the discrete spaces: $\mathbf{W}_h^{\text{DG}} = \text{span}\{\varphi_{\text{el}}^i\}_{i=0}^{N_{\text{el}}}$, $\mathbf{V}_h^{\text{DG}} = \text{span}\{\varphi_{\text{el}}^i\}_{i=0}^{N_{\text{f}}}$.

6 Verification of convergence estimates

To verify the theoretical error estimates of Theorem 2 and the implemented solver, we report convergence tests on a simplified mesh made of two juxtaposed unit cubes $\Omega_{\text{f}} = (0, 1) \times (1, 0) \times (-1, 0), \Omega_{\text{el}} = (0, 1)^3$, where the interface is $\Sigma = \{\mathbf{x} = (x, y, z): z = 0, (x, y) \in (0, 1)^2\}$. Considering only one fluid compartment in the poroelastic system, namely $J = \{\text{E}\}$, and setting all physical coefficients of Table 1 to be equal to 1, except for $\alpha_{\text{E}} = 0.5$, the following is an exact solution of problem (1)-(2) for suitable expressions of the source functions $\mathbf{f}_{\text{el}}, g_{\text{E}}, \mathbf{f}_{\text{f}}$, the boundary data, and the initial conditions $\mathbf{d}_0, \dot{\mathbf{d}}_0, p_{\text{E}0}, \mathbf{u}_0$:

$$\mathbf{u}(\mathbf{x}, t) = (2t - t^2)e^{-t} \begin{bmatrix} y^M z^M \\ x^M z^M \\ \xi \end{bmatrix}, \quad \mathbf{d}(\mathbf{x}, t) = t^2 e^{-t} \begin{bmatrix} y^M z^M \\ x^M z^M \\ -\xi \end{bmatrix}, \quad (16)$$

$$p(\mathbf{x}, t) = p_{\text{E}}(\mathbf{x}, t) = (1 - e^{-t})z^M.$$

In particular, we choose $M = 5$ and $\xi = 1$ and impose Dirichlet conditions for all variables on the whole of $\partial\Omega$.

We simulate 5 time steps with step length $\Delta t = 10^{-3}$, chosen small enough to avoid spoiling convergence w.r.t. space discretization. In Fig. 3, we report the computed errors in the energy norm (9). The results agree with the convergence order $h^m, m = 1, 2, 3$ predicted by Theorem 2.

7 Application to brain fluid-poromechanics: physiological conditions in idealized geometry

In this section, we consider the CSF modeling by the Stokes equations (namely we neglect the nonlinear advection term in (2)) and we apply our multi-physics model to physiological settings, focusing on the CSF compartment. Specifically, we consider $J = \{\text{E}\}$ and the values of the physical parameters reported in Table 1, with typical physiological values according to [6, 40, 41].

The only non-zero distributed source/sink term is g_{E} , whereas $\mathbf{f}_{\text{el}}, \mathbf{f}_{\text{f}}$ are set to zero. This non-zero function is homogenous in space, and its dependence on time is $g_{\text{E}}(t) = 0.2\pi \sin(2\pi t)$, corresponding to an overall inflow $Q_{\text{in}}(t) = |\Omega_{\text{el}}|g_{\text{E}}(t)$ which is in the range of the CSF generation rate in physiological conditions: cfr. [6, 5].

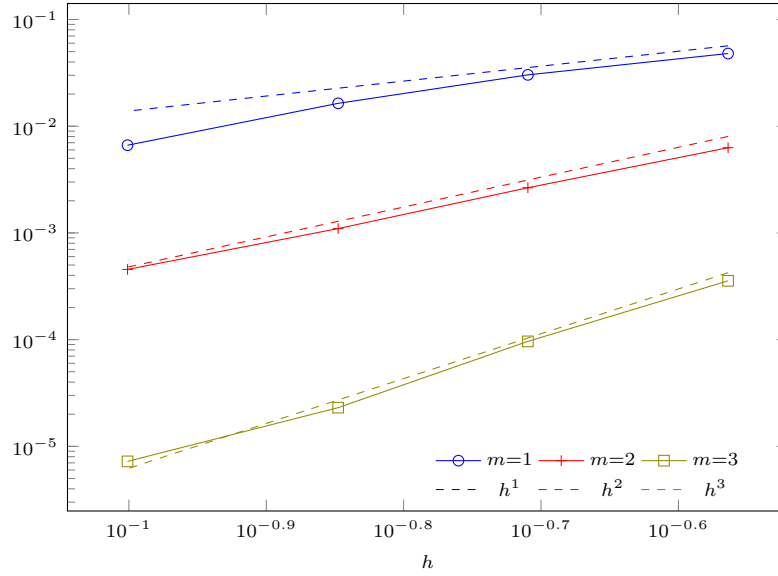


Figure 3: Verification test: computed relative errors in the energy norm (9) against h in log-log scale, with different polynomial degrees m .

parameter	phys. values	description
ρ_{el}, ρ_f	$1000 \text{ kg} \cdot \text{m}^{-3}$	density of the solid tissue and of the CSF
μ_{el}	216 Pa	first Lamé parameter of the solid
λ	$11\,567 \text{ Pa}$	second Lamé parameter of the solid
μ_E, μ_f	$3.5 \cdot 10^{-3} \text{ Pa} \cdot \text{s}$	viscosity of the fluid in compartment E and of CSF
α_E	0.49	Biot-Willis coefficient of compartment E
c_E	$10^{-6} \text{ m}^2 \cdot \text{N}^{-1}$	storage coefficient of compartment E
\tilde{k}_E	10^{-16} m^2	$k_E = \tilde{k}_E I$ permeability tensor for compartment E
β_E^e	$0 \text{ m}^2 \cdot \text{N}^{-1} \cdot \text{s}^{-1}$	external coupling coefficient for compartment $E \in J$
γ	1	non-dimensional slip rate coefficient at interface Σ

Table 1: Parameters of model (2) with corresponding physiological values [6, 40, 41].

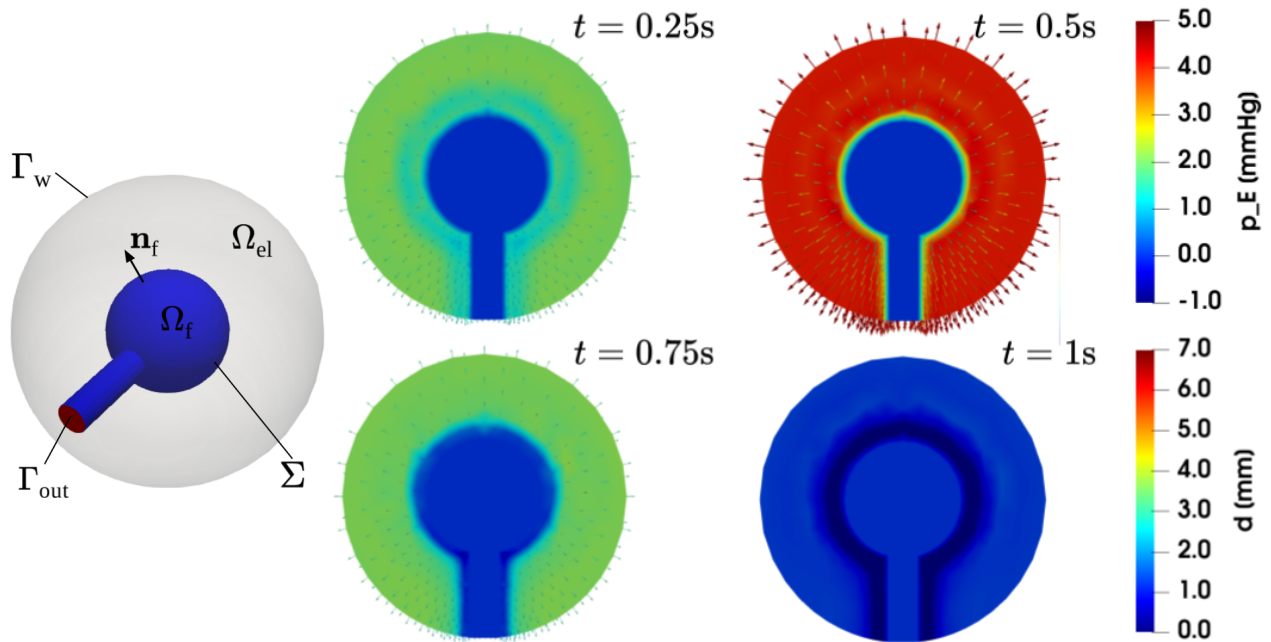


Figure 4: Test case of Section 7. Left: computational domain and boundaries. Right: longitudinal clip with computed displacement \mathbf{d}_h and interstitial pressures $p_{E,h}$, for different time snapshots.

The idealized geometry displayed in Fig. 4, left, retains the same topology of the brain and CSF system: the porous tissue is contained in Ω_{el} , while the CSF can flow in the ventricle system Ω_f , including a duct connecting it to the spinal canal at Γ_{out} . The volumes of the poroelastic and fluid domains at rest are $|\Omega_{el}| = 9.68$ mL and $|\Omega_f| = 0.89$ mL, respectively. The corresponding mesh is made of $N = 16834$ elements with an average size $h = 1.6$ mm. In terms of boundary conditions, on the outflow Γ_{out} we prescribe the CSF pressure $\bar{p}^{out} = 0$ and on the outer wall Γ_w we impose no traction on the tissue and no flow of the extracellular CSF. To ensure that the periodic regime is attained, we simulate 3 periods of the source term g_E , of duration $T = 1$ s, using a time step $\Delta t = 10^{-3}$ s. In the following, all results refer to the third period, with time $t = 0$ set at its beginning.

The displacement \mathbf{d}_h and the interstitial CSF pressure $p_{E,h}$ are reported in Fig. 4, for selected time snapshots. The magnitude of \mathbf{d}_h , reaching its peak at $t = 0.5$ s, never exceeds 6.6 mm, thus it justifies the choice of a linear elastic model for the cerebral tissue, in these settings. Regarding $p_{E,h}$, at the same peak time $t = 0.5$ s we observe a maximum difference of 4.4 mmHg between the outer boundary Γ_{out} and the interface Σ , which is comparable with analogous simulations in brain geometries [6, 33]. We also observe that a slight phase displacement occurs in the late part of the period between $p_{E,h}$ and the data g_E , with a minimum of -1.9 mmHg attained at $t = 0.94$ s: this is due to the inertial properties of the system, which are going to be discussed in Section 8.

Regarding the CSF velocity \mathbf{u}_h and pressure p_h in the Stokes domain Ω_f , the results are reported in Fig. 5. The pressure gradient is significantly smaller than in the poroelastic medium and the velocity magnitude is in the physiological range reported in clinical measurements and computational assessments in the cerebral aqueduct [6, 5]. The positive and increasing pressure gradient observed in the final portion of the period (see Fig. 5, $t = 1$ s) is due to the aforementioned inertial effects, even more noticeable in the flowrate plots of Fig. 6, where the output flowrate $Q_{out} = \int_{\Gamma_{out}} \mathbf{u}_h \cdot \mathbf{n} d\Gamma$ shows a significant phase displacement w.r.t. the inflow $Q_{in} = \int_{\Omega_E} g_E d\Omega = |\Omega_E| g_E$ associated to the source term.

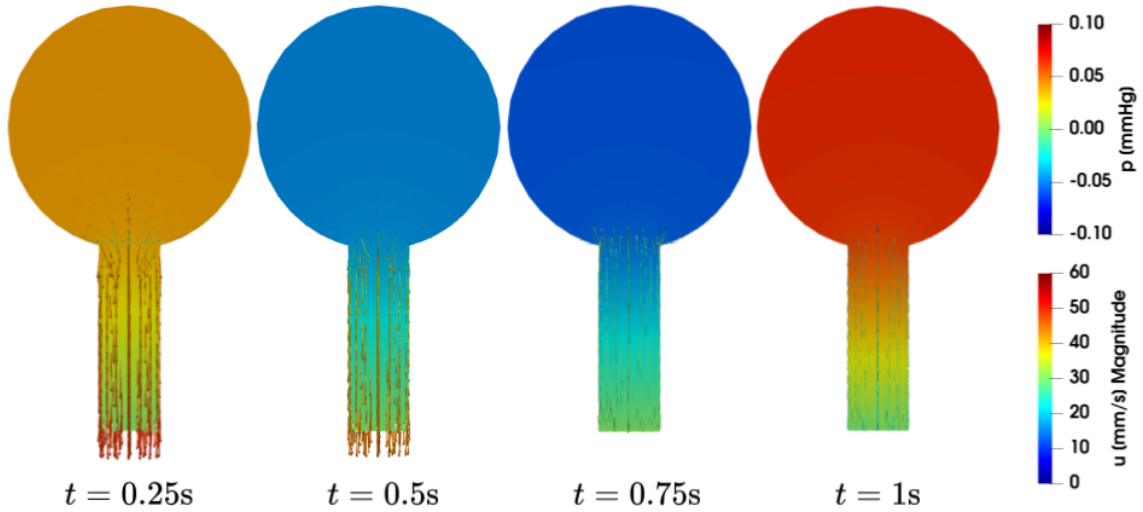


Figure 5: Test case of Section 7: longitudinal clip. Computed velocity \mathbf{u}_h and pressures p_h in the fluid domain Ω_f , for different time snapshots.

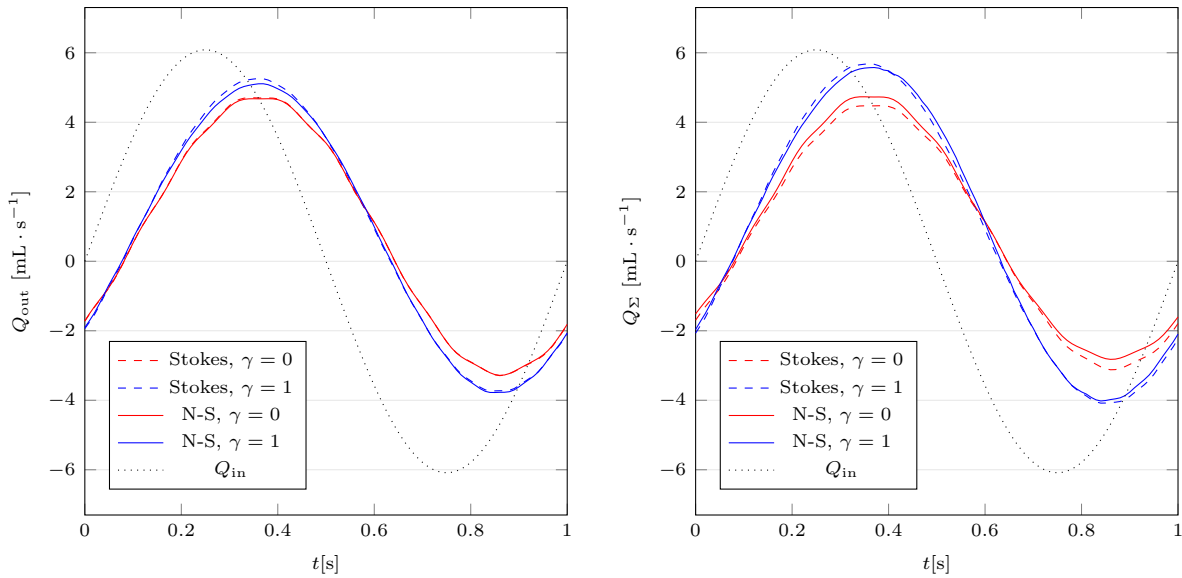


Figure 6: Test cases of Sections 7 and 8. Computed flowrates over a period, for different modeling choices (N-S: Navier-Stokes). Left: outlet flowrate $Q_{\text{out}} = \int_{\Gamma_{\text{out}}} \mathbf{u}_h \cdot \mathbf{n}$; right: interface flowrate $Q_{\Sigma} = \int_{\Sigma} \mathbf{u}_h \cdot \mathbf{n}_{\text{el}}$. In both: distributed CSF inflow flowrate $Q_{\text{in}} = \int_{\Omega_{\text{el}}} g_E$ for reference.

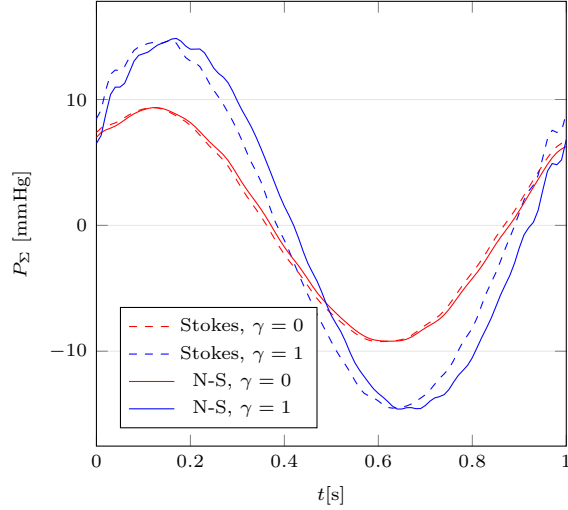


Figure 7: Test cases of Sections 7 and 8. Interface-average fluid pressure $P_\Sigma = \frac{1}{|\Sigma|} \int_\Sigma p_h$ over a period for different modeling choices (N-S: Navier-Stokes).

8 Application to brain poro-mechanics: effects of BJS conditions and advection term

This section aims to assess the effects of the modeling choices for the advection term in the fluid part of system (2) – namely either Stokes or Navier-Stokes equations – and of the BJS condition (1e) at the interface – namely either $\gamma = 0$ or $\gamma = 1$. Since a semi-implicit treatment of the advection term is employed, as reported in (13), the problem to be solved at each time step is linear also in the Navier-Stokes case. Moreover, backflow stabilization is needed in the Navier-Stokes case for the latest portion of the period: the term $\int_{\Gamma_{\text{out}}} \frac{\rho_f}{2} \min\{0, \mathbf{u}_h^n \cdot \mathbf{n}\} \mathbf{u}_h^{n+1} \cdot \mathbf{v}_h$ is added to the left-hand side of the fully discrete problem (14) [42].

Observing the outlet flowrate Q_{out} and the interface flowrate $Q_\Sigma = \int_\Sigma \mathbf{u}_h \cdot \mathbf{n}_{\text{el}}$ displayed in Fig. 6, we can notice that the differences are negligible between the Stokes and Navier-Stokes case (for the same value of γ). Indeed, the outlet Reynolds number $\text{Re} = \frac{\rho_f Q_{\text{out}}}{\mu_f \pi D}$, D being the diameter of the circular outlet section Γ_{out} , is in the range (40, 50) for all cases.

A slight phase difference between the Stokes and Navier-Stokes model can, instead, be appreciated in the interface-averaged pressure $P_\Sigma = \frac{1}{|\Sigma|} \int_\Sigma p_h$ reported in Fig. 7, particularly in the case $\gamma = 1$ corresponding to BJS conditions: this difference can be ascribed to the additional inertia accounted for by the advection term in Navier-Stokes equations. Overall, the results discussed here quantitatively show that the choice of the simpler Stokes model is definitely enough to represent the flow in the regime of interest, which is the one of CSF flow in the cerebral ventricles.

To assess the effects of the BJS condition (1e), we can compare the cases $\gamma = 0$ (no tangential stress at the pores) to the cases $\gamma = 1$ (BJS condition) in Figs. 6 and 7. The approximately sinusoidal evolution of flowrates and pressure exhibits a smaller amplitude in the case $\gamma = 0$, particular significant in the interface quantities Q_Σ and P_Σ . An interpretation of this effect is that the friction in the tangential direction introduced by the BJS interface condition makes CSF velocity orient in the direction orthogonal to the interface, thus increasing the amount of CSF flowing through it at each given time. Due to the incompressibility of the fluid model, this increased flow corresponds to an increased pressure difference $P_\Sigma - \bar{p}_{\text{out}} = P_\Sigma$. This is confirmed by the results reported in Fig. 8: when the BJS condition is applied, \mathbf{u}_h is mostly normal to the interface in the upper region of Ω_f (see the boxed panels in Fig. 8), and an increased flowrate is observable in the vertical duct representing the cerebral aqueduct. Moreover, the friction

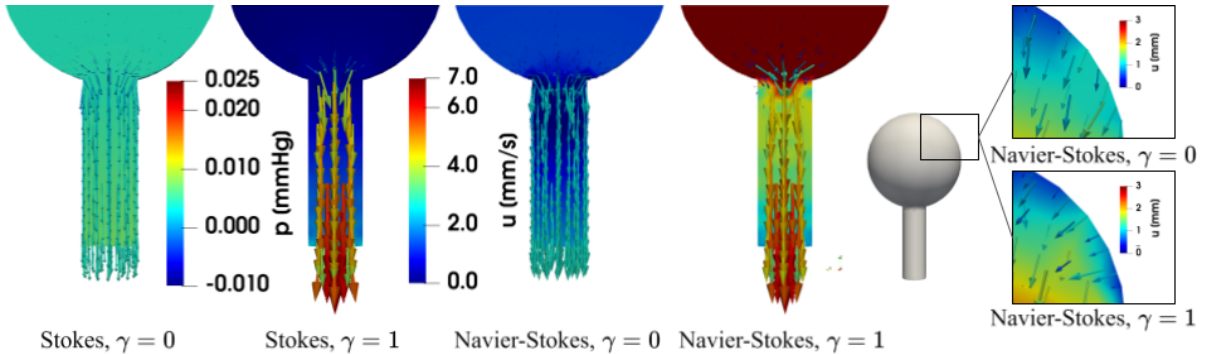


Figure 8: Test cases of Sections 7 and 8: longitudinal clip. Main panels: computed velocity \mathbf{u}_h and pressures p_h in the fluid domain Ω_f at $t = 0.24$ s, for different modeling choices. Right: zoom on \mathbf{u}_h distribution in the boxed region.

introduced by the BJS condition yields an approximately parabolic profile in the duct, in contrast with the flat profile of the case $\gamma = 0$. Such a parabolic profile better represents the actual CSF flow in the cerebral aqueduct [43]. To conclude this discussion, it is interesting to notice that, despite the significant differences in the pressure and velocity distribution, the outlet flowrate Q_{out} shows little discrepancies between the different cases, since the outflow is mostly driven by conservation of mass.

9 Conclusions

Motivated by the modeling of cerebrospinal fluid (CSF) flow in the brain, in this work we studied a coupled multi-domain system encompassing multiple-network poroelasticity and (Navier-)Stokes equations, with a particular focus on the interface conditions between the two physical domains. The polytopal discontinuous Galerkin method for space discretization introduced in [33] was extended to consider the nonlinear advection term of Navier-Stokes equations in the fluid domain and Beavers-Joseph-Saffman (BJS) interface conditions: an a priori analysis of the resulting method in the Stokes case proved it to be stable and optimally convergent. The method was also numerically verified by means of convergence tests in three dimensions. Considering an idealized geometry, representative of the main topological characteristics of the brain tissue and ventricular system, the method was employed to represent porous tissue dynamics and CSF flow in physiological settings, obtaining results in partial consistency with the literature. Analyzing the effects of the advection term in the fluid model, it was quantitatively observed that neglecting the advection term in the Navier-Stokes equations does not have a significant impact on the CSF velocity distribution (at least in physiological conditions), though it may yield a slightly inaccurate prediction of the pressure distribution. Finally, it was highlighted how the BJS condition strongly affects the CSF pressure and velocity distribution: the results obtained with the enforcement of this condition better represent the CSF flow in the brain, especially in terms of its profile in the cerebral aqueduct.

To further develop the computational model proposed in this work, its application to patient-specific geometries could be considered, to allow a detailed investigation of the waste clearance mechanisms of the brain function. In this direction, image segmentation pipelines developed in the literature (see, e.g., [44, 45]) should be combined with mesh generation and agglomeration algorithms for the construction of a polyhedral mesh [46, 47, 48]. Moreover, the multiple-network modeling of tissue perfusion could be exploited to assimilate clinical measurements of the blood flow in the cerebral vasculature directly into the model, without the need for a pre-processing phase to estimate CSF generation from such data, or to combine the system with more detailed computational models of the heart pulsation [49, 50, 51]. Finally, an extension to more complex hyperelastic rheologies of the brain tissue should be envisaged, to more accurately represent its mechanical response [52].

Acknowledgments

The author would like to thank Paola F. Antonietti and Nicola Parolini for the fruitful discussions. The author has been supported by *ICSC–Centro Nazionale di Ricerca in High Performance Computing, Big Data, e Quantum Computing* funded by the European Union–NextGenerationEU. The present research is part of the activities of “Dipartimento di Eccellenza 2023-2027”, Dipartimento di Matematica, Politecnico di Milano. The author is member of GNCS-INdAM and acknowledges the support of the GNCS project CUP E53C23001670001.

A Bilinear forms and functionals of the semi-discrete problem

The forms building up the semidiscrete problem (7) are defined as follows:

$$\mathcal{L}_{\text{el}}(\mathbf{d}, \{p_k\}_{k \in J}; \mathbf{w}) = \mathcal{A}_{\text{el}}(\mathbf{d}, \mathbf{w}) + \sum_{k \in J} \mathcal{B}_k(p_k, \mathbf{w}), \quad (17a)$$

$$\mathcal{L}_j(\{p_k\}_{k \in J}, \partial_t \mathbf{d}; q_j) = \mathcal{A}_j(p_j, q_j) + \mathcal{C}_j(\{p_k\}_{k \in J}, q_j) - \mathcal{B}_j(q_j, \partial_t \mathbf{d}), \quad \forall j \in J, \quad (17b)$$

$$\mathcal{L}_f(\mathbf{u}, p; \mathbf{v}, q) = \mathcal{N}_f(\mathbf{u}, \mathbf{u}, \mathbf{v}) + \mathcal{A}_f(\mathbf{u}, \mathbf{v}) + \mathcal{B}_f(p, \mathbf{v}) - \mathcal{B}_f(q, \mathbf{u}) + \mathcal{S}(p, q), \quad (17c)$$

where

$$\begin{aligned} \mathcal{A}_{\text{el}}(\mathbf{d}, \mathbf{w}) &= \int_{\Omega_{\text{el}}} \sigma_{\text{el}}(\mathbf{d}) : \varepsilon_h(\mathbf{w}) \\ &\quad - \sum_{F \in \mathcal{F}_{\text{el}}^1 \cup \mathcal{F}_{\text{el}}^{\text{D}}} \int_F (\{\{\sigma_{\text{el}}(\mathbf{d})\}\} : \llbracket \mathbf{w} \rrbracket + \llbracket \mathbf{d} \rrbracket : \{\{\sigma_{\text{el}}(\mathbf{w})\}\} - \eta \llbracket \mathbf{d} \rrbracket : \llbracket \mathbf{w} \rrbracket), \end{aligned} \quad (18a)$$

$$\mathcal{F}_{\text{el}}(\mathbf{w}) = \int_{\Omega_{\text{el}}} \mathbf{f}_{\text{el}} \cdot \mathbf{w}, \quad (18b)$$

$$\mathcal{B}_j(p_j, \mathbf{w}) = - \int_{\Omega_{\text{el}}} \alpha_j p_j \operatorname{div}_h \mathbf{w} + \sum_{F \in \mathcal{F}_{\text{el}}^1 \cup \mathcal{F}_{\text{el}}^{\text{D}_j}} \int_F \alpha_j \{\{p_j I\}\} : \llbracket \mathbf{w} \rrbracket, \quad (18c)$$

$$\begin{aligned} \mathcal{A}_j(p_j, q_j) &= \int_{\Omega_{\text{el}}} \mu_j^{-1} k_j \nabla_h p_j \cdot \nabla_h q_j \\ &\quad - \sum_{F \in \mathcal{F}_{\text{el}}^1 \cup \mathcal{F}_{\text{el}}^{\text{D}_j}} \int_F (\{\{\mu_j^{-1} k_j \nabla_h p_j\}\} \cdot \llbracket q_j \rrbracket + \llbracket p_j \rrbracket \cdot \{\{\mu_j^{-1} k_j \nabla_h q_j\}\} - \zeta_j \llbracket p_j \rrbracket \cdot \llbracket q_j \rrbracket), \end{aligned} \quad (18d)$$

$$\mathcal{C}_j(\{p_k\}_{k \in J}, q_j) = \int_{\Omega_{\text{el}}} \sum_{k \in J} \beta_{kj} (p_j - p_k) q_j + \int_{\Omega_{\text{el}}} \beta_j^e p_j q_j, \quad (18e)$$

$$\mathcal{F}_j(q_j) = \int_{\Omega_{\text{el}}} g_j q_j, \quad (18f)$$

$$\begin{aligned} \mathcal{A}_f(\mathbf{u}, \mathbf{v}) &= \int_{\Omega_f} \tau_f(\mathbf{u}) : \varepsilon_h(\mathbf{v}) \\ &\quad - \sum_{F \in \mathcal{F}_f^I \cup \mathcal{F}_f^D} \int_F (\{\tau_f(\mathbf{u})\} : \llbracket \mathbf{v} \rrbracket + \llbracket \mathbf{u} \rrbracket : \{\tau_f(\mathbf{v})\} - \gamma_v \llbracket \mathbf{u} \rrbracket : \llbracket \mathbf{v} \rrbracket), \end{aligned} \quad (19a)$$

$$\begin{aligned} \mathcal{N}_f(\mathbf{u}', \mathbf{u}, \mathbf{v}) &= \int_{\Omega_f} \left(\rho_f(\mathbf{u}' \cdot \nabla_h) \mathbf{u} \cdot \mathbf{v} + \frac{\rho_f}{2} (\nabla_h \cdot \mathbf{u}') \mathbf{u} \cdot \mathbf{v} \right) \\ &\quad - \sum_{F \in \mathcal{F}_f^I} \int_F \left(\rho_f \llbracket \mathbf{u} \rrbracket : \{\mathbf{u}'\} \otimes \{\mathbf{v}\} + \frac{\rho_f}{2} \llbracket \mathbf{u}' \rrbracket : I \{\mathbf{u} \cdot \mathbf{v}\} \right), \end{aligned} \quad (19b)$$

$$\mathcal{B}_f(p, \mathbf{v}) = - \int_{\Omega_f} p \operatorname{div}_h \mathbf{v} + \sum_{F \in \mathcal{F}_f^I \cup \mathcal{F}_f^D} \int_F \{\{pI\}\} : \llbracket \mathbf{v} \rrbracket, \quad (19c)$$

$$\mathcal{F}_f(\mathbf{v}) = \int_{\Omega_f} \mathbf{f}_f \cdot \mathbf{v}, \quad (19d)$$

$$\mathcal{S}(p, q) = \sum_{F \in \mathcal{F}_f^I} \int_F \gamma_p \llbracket p \rrbracket \cdot \llbracket q \rrbracket, \quad (19e)$$

$$\mathcal{J}(p_E, \mathbf{w}, \mathbf{v}) = \sum_{F \in \mathcal{F}_\Sigma} \int_F (\{\{p_E I\}\} : \llbracket \mathbf{w}, \mathbf{v} \rrbracket), \quad (19f)$$

$$\mathcal{G}(\mathbf{v}_1 - \mathbf{w}_1, \mathbf{v}_2 - \mathbf{w}_2) = \sum_{F \in \mathcal{F}_\Sigma} \int_F \frac{\gamma_{\mu_f}}{\sqrt{k_E}} \llbracket \mathbf{w}_1, \mathbf{v}_1 \rrbracket_\tau \cdot \llbracket \mathbf{w}_2, \mathbf{v}_2 \rrbracket_\tau, \quad (19g)$$

where $\nabla_h, \varepsilon_h, \operatorname{div}_h$ denote the element-wise gradient, symmetric gradient, and divergence operators, respectively, and the stress tensors $\sigma_{\text{el}}, \tau_f$ are implicitly defined in terms of these piecewise operators. The parameters $\eta, \zeta_j, \gamma_v, \gamma_p$ appearing in these forms are defined as follows [11, 15]:

$$\eta = \bar{\eta} \frac{\bar{\mathbb{C}}_{\text{el}}^K}{\{h\}_{\text{H}}}, \quad \zeta_j = \bar{\zeta}_j \frac{\bar{k}_j^K}{\sqrt{\mu_j} \{h\}_{\text{H}}}, \quad \gamma_v = \bar{\gamma}_v \frac{\mu}{\{h\}_{\text{H}}}, \quad \gamma_p = \bar{\gamma}_p \{h\}_{\text{H}}, \quad (20)$$

where $\{h\}_{\text{H}}$ denotes the harmonic average on K^\pm (with $\{h\}_{\text{H}} = h_K$ on Dirichlet faces), $\bar{\mathbb{C}}_{\text{el}}^K = \|\mathbb{C}_{\text{el}}^{1/2}|_K\|_2^2$ and $\bar{k}_j^K = \|k_j^{1/2}|_K\|_2^2$ are the L^2 -norms of the symmetric second-order tensors appearing in the elasticity and Darcy equations, for each $K \in \mathcal{T}_{h,\text{el}}$, and $\bar{\eta}, \bar{\zeta}_j \forall j \in J, \bar{\gamma}_v, \bar{\gamma}_p$ are penalty constants to be chosen large enough. In all the numerical tests of the present work, all these penalty constants are set to 10.

B Stein interpolation results

If Ω is a Lipschitz-regular domain, the following interpolation results hold for the Stein extension operator $\mathcal{E}_K : H^s(\Omega) \rightarrow H^s(\mathbb{R}^d)$ (cf. [33, 53]):

Lemma 1 *Under Assumption 1, the following estimates hold:*

$$\begin{aligned}
& \forall (\mathbf{w}, \{q_j\}_{j \in J}, \mathbf{v}, q) \in [H^{m+1}(\mathcal{T}_{h,el})]^{d+N_J} \times [H^{m+1}(\mathcal{T}_{h,f})]^{d+1} \\
& \exists (\mathbf{w}_I, \{q_{jI}\}_{j \in J}, \mathbf{v}_I, q_I) \in \mathbf{W}_h^{\text{DG}} \times [Q_{J,h}^{\text{DG}}]^{N_J} \times \mathbf{V}_h^{\text{DG}} \times Q_h^{\text{DG}} \quad \text{such that} \\
& i) \quad \left\| (\mathbf{w} - \mathbf{w}_I, \{q_j - q_{jI}\}_{j \in J}, \mathbf{v} - \mathbf{v}_I, q - q_I) \right\|^2 \\
& \quad \lesssim \sum_{K \in \mathcal{T}_{h,el}} h_K^{2m} \left(\|\mathcal{E}_K \mathbf{w}\|_{[H^{m+1}(\hat{K})]^d}^2 + \sum_{j \in J} \|\mathcal{E}_j q_j\|_{H^{m+1}(\hat{K})}^2 + \|\mathcal{E}_K \mathbf{d}\|_{[H^{m+1}(\hat{K})]^d}^2 + \|\mathcal{E}_K p\|_{H^{m+1}(\hat{K})}^2 \right), \\
& ii) \quad \|\mathbf{w}\|_{\mathcal{F}\Sigma}^2 + \sum_{j \in J} \|q_j\|_{\mathcal{F}\Sigma}^2 + \|\mathbf{v}\|_{\mathcal{F}\Sigma}^2 + \|q\|_{\mathcal{F}\Sigma}^2 \\
& \quad \lesssim \sum_{K \in \mathcal{T}_{h,el}} h_K^{2m+1} \left(\|\mathcal{E}_K \mathbf{w}\|_{[H^{m+1}(\hat{K})]^d}^2 + \sum_{j \in J} \|\mathcal{E}_j q_j\|_{H^{m+1}(\hat{K})}^2 + \|\mathcal{E}_K \mathbf{d}\|_{[H^{m+1}(\hat{K})]^d}^2 + \|\mathcal{E}_K p\|_{H^{m+1}(\hat{K})}^2 \right),
\end{aligned}$$

where $\hat{K} \supseteq K$, for each $K \in \mathcal{T}_h$, are shape-regular simplexes covering \mathcal{T}_h , thanks to Assumption 1.

References

- [1] W. J. Layton, F. Schieweck, I. Yotov, Coupling fluid flow with porous media flow, *SIAM Journal on Numerical Analysis* 40 (6) (2002) 2195–2218.
- [2] M. Discacciati, E. Miglio, A. Quarteroni, Mathematical and numerical models for coupling surface and ground-water flows, *Applied Numerical Mathematics* 43 (1-2) (2002) 57–74.
- [3] C. Michler, A. N. Cookson, R. Chabiniok, E. Hyde, J. Lee, M. Sinclair, T. Sochi, A. Goyal, G. Viguera, D. Nordsletten, et al., A computationally efficient framework for the simulation of cardiac perfusion using a multi-compartment Darcy porous-media flow model, *International journal for numerical methods in biomedical engineering* 29 (2) (2013) 217–232.
- [4] S. Di Gregorio, M. Fedele, G. Pontone, A. F. Corno, P. Zunino, C. Vergara, A. Quarteroni, A computational model applied to myocardial perfusion in the human heart: from large coronaries to microvasculature, *Journal of Computational Physics* 424 (2021) 109836.
- [5] O. Balédent, I. Idy-Peretti, et al., Cerebrospinal fluid dynamics and relation with blood flow: a magnetic resonance study with semiautomated cerebrospinal fluid segmentation, *Investigative radiology* 36 (7) (2001) 368–377.
- [6] M. Causemann, V. Vinje, M. E. Rognes, Human intracranial pulsatility during the cardiac cycle: a computational modelling framework, *Fluids and Barriers of the CNS* 19 (1) (2022) 1–17.
- [7] L. M. Hablitz, M. Nedergaard, The glymphatic system, *Current Biology* 31 (20) (2021) R1371–R1375.
- [8] G. S. Brennan, T. B. Thompson, H. Oliveri, M. E. Rognes, A. Goriely, The role of clearance in neurodegenerative diseases, *SIAM Journal on Applied Mathematics* (2023) S172–S198.
- [9] A. Bacyinski, M. Xu, W. Wang, J. Hu, The paravascular pathway for brain waste clearance: current understanding, significance and controversy, *Frontiers in neuroanatomy* 11 (2017) 101.
- [10] L. Guo, J. C. Vardakis, T. Lassila, M. Mitolo, N. Ravikumar, D. Chou, M. Lange, A. Sarrami-Foroushani, B. J. Tully, Z. A. Taylor, et al., Subject-specific multi-poroelastic model for exploring the risk factors associated with the early stages of alzheimer’s disease, *Interface focus* 8 (1) (2018) 20170019.
- [11] M. Corti, P. F. Antonietti, L. Dede’, A. M. Quarteroni, Numerical modelling of the brain poromechanics by high-order discontinuous Galerkin methods, *Mathematical Models and Methods in Applied Sciences* 33 (8) (2023) 1577–1609.
- [12] S. Sun, M. F. Wheeler, Symmetric and nonsymmetric discontinuous Galerkin methods for reactive transport in porous media, *SIAM Journal on Numerical Analysis* 43 (1) (2005) 195–219.

- [13] K. Lipnikov, D. Vassilev, I. Yotov, Discontinuous Galerkin and mimetic finite difference methods for coupled Stokes–Darcy flows on polygonal and polyhedral grids, *Numerische Mathematik* 126 (2) (2014) 321–360.
- [14] J. Li, B. Riviere, High order discontinuous Galerkin method for simulating miscible flooding in porous media, *Computational Geosciences* 19 (2015) 1251–1268.
- [15] P. F. Antonietti, L. Mascotto, M. Verani, S. Zonca, Stability analysis of polytopic discontinuous Galerkin approximations of the Stokes problem with applications to fluid–structure interaction problems, *Journal of Scientific Computing* 90 (2022) 1–31.
- [16] H. H. Kim, E. T. Chung, C. S. Lee, A staggered discontinuous Galerkin method for the Stokes system, *SIAM Journal on Numerical Analysis* 51 (6) (2013) 3327–3350.
- [17] S. W. Cheung, E. Chung, H. H. Kim, Y. Qian, Staggered discontinuous Galerkin methods for the incompressible Navier–Stokes equations, *Journal of Computational Physics* 302 (2015) 251–266.
- [18] L. Zhao, E. T. Chung, E.-J. Park, G. Zhou, Staggered DG method for coupling of the Stokes and Darcy–Forchheimer problems, *SIAM Journal on Numerical Analysis* 59 (1) (2021) 1–31.
- [19] D. Boffi, M. Botti, D. A. Di Pietro, A nonconforming high-order method for the Biot problem on general meshes, *SIAM Journal on Scientific Computing* 38 (3) (2016) A1508–A1537.
- [20] D. Anderson, J. Droniou, An arbitrary-order scheme on generic meshes for miscible displacements in porous media, *SIAM Journal on Scientific Computing* 40 (4) (2018) B1020–B1054.
- [21] L. Botti, M. Botti, D. A. Di Pietro, A hybrid high-order method for multiple-network poroelasticity, in: *Polyhedral methods in geosciences*, Springer, 2021, pp. 227–258.
- [22] S. Badia, A. Quaini, A. Quarteroni, Coupling Biot and Navier–Stokes equations for modelling fluid–poroelastic media interaction, *Journal of Computational Physics* 228 (21) (2009) 7986–8014.
- [23] I. Ambartsumyan, E. Khattatov, I. Yotov, P. Zunino, A Lagrange multiplier method for a Stokes–Biot fluid–poroelastic structure interaction model, *Numerische Mathematik* 140 (2) (2018) 513–553.
- [24] J. Wen, Y. He, A strongly conservative finite element method for the coupled Stokes–Biot model, *Computers & Mathematics with Applications* 80 (5) (2020) 1421–1442.
- [25] K.-A. Mardal, M. E. Rognes, T. B. Thompson, Accurate discretization of poroelasticity without Darcy stability: Stokes–Biot stability revisited, *BIT Numerical Mathematics* 61 (2021) 941–976.
- [26] A. Dereims, S. Drapier, J.-M. Bergheau, P. De Luca, 3D robust iterative coupling of Stokes, Darcy and solid mechanics for low permeability media undergoing finite strains, *Finite Elements in Analysis and Design* 94 (2015) 1–15.
- [27] L. Bociu, S. Canic, B. Muha, J. T. Webster, Multilayered poroelasticity interacting with Stokes flow, *SIAM Journal on Mathematical Analysis* 53 (6) (2021) 6243–6279.
- [28] M. Bukač, I. Yotov, P. Zunino, An operator splitting approach for the interaction between a fluid and a multilayered poroelastic structure, *Numerical Methods for Partial Differential Equations* 31 (4) (2015) 1054–1100.
- [29] N. A. Barnafi Wittwer, S. D. Gregorio, L. Dede, P. Zunino, C. Vergara, A. Quarteroni, A multiscale poromechanics model integrating myocardial perfusion and the epicardial coronary vessels, *SIAM Journal on Applied Mathematics* 82 (4) (2022) 1167–1193.
- [30] D. Chou, J. C. Vardakis, L. Guo, B. J. Tully, Y. Ventikos, A fully dynamic multi-compartmental poroelastic system: Application to aqueductal stenosis, *Journal of Biomechanics* 49 (11) (2016) 2306–2312.
- [31] J. J. Lee, E. Piersanti, K.-A. Mardal, M. E. Rognes, A mixed finite element method for nearly incompressible multiple-network poroelasticity, *SIAM journal on scientific computing* 41 (2) (2019) A722–A747.
- [32] E. Eliseussen, M. E. Rognes, T. B. Thompson, A posteriori error estimation and adaptivity for multiple-network poroelasticity, *ESAIM: Mathematical Modelling and Numerical Analysis* 57 (4) (2023) 1921–1952.

- [33] I. Fumagalli, M. Corti, N. Parolini, P. F. Antonietti, Polytopal discontinuous Galerkin discretization of brain multiphysics flow dynamics, *Journal of Computational Physics* (2024) 113115.
- [34] P. G. Saffman, On the boundary condition at the surface of a porous medium, *Studies in applied mathematics* 50 (2) (1971) 93–101.
- [35] I. N. Drøsdal, K.-A. Mardal, K. Støverud, V. Haughton, Effect of the central canal in the spinal cord on fluid movement within the cord, *The neuroradiology journal* 26 (5) (2013) 585–590.
- [36] R. Temam, *Navier-Stokes equations: theory and numerical analysis*, Vol. 343, American Mathematical Soc., 2001.
- [37] P. F. Antonietti, A. Cangiani, J. Collis, Z. Dong, E. H. Georgoulis, S. Giani, P. Houston, Review of discontinuous Galerkin finite element methods for partial differential equations on complicated domains, *Building bridges: connections and challenges in modern approaches to numerical partial differential equations* (2016) 281–310.
- [38] A. Cangiani, E. H. Georgoulis, P. Houston, hp-version discontinuous Galerkin methods on polygonal and polyhedral meshes, *Mathematical Models and Methods in Applied Sciences* 24 (10) (2014) 2009–2041.
- [39] E. M. Stein, *Singular integrals and differentiability properties of functions*, Princeton university press, 1970.
- [40] K. E. Holter, B. Kehlet, A. Devor, T. J. Sejnowski, A. M. Dale, S. W. Omholt, O. P. Ottersen, E. A. Nagelhus, K.-A. Mardal, K. H. Pettersen, Interstitial solute transport in 3d reconstructed neuropil occurs by diffusion rather than bulk flow, *Proceedings of the National Academy of Sciences* 114 (37) (2017) 9894–9899.
- [41] J. Tithof, K. A. Boster, P. A. Bork, M. Nedergaard, J. H. Thomas, D. H. Kelley, A network model of glymphatic flow under different experimentally-motivated parametric scenarios, *IScience* 25 (5) (2022).
- [42] M. Esmaily Moghadam, Y. Bazilevs, T.-Y. Hsia, I. E. Vignon-Clementel, A. L. Marsden, M. of Congenital Hearts Alliance (MOCHA), A comparison of outlet boundary treatments for prevention of backflow divergence with relevance to blood flow simulations, *Computational Mechanics* 48 (2011) 277–291.
- [43] B. Sweetman, M. Xenos, L. Zitella, A. A. Linninger, Three-dimensional computational prediction of cerebrospinal fluid flow in the human brain, *Computers in biology and medicine* 41 (2) (2011) 67–75.
- [44] K.-A. Mardal, M. E. Rognes, T. B. Thompson, L. M. Valnes, *Mathematical modeling of the human brain: from magnetic resonance images to finite element simulation*, Springer Nature, 2022.
- [45] I. Fumagalli, M. Fedele, C. Vergara, L. Dede’, S. Ippolito, F. Nicolò, C. Antona, R. Scrofani, A. Quarteroni, An image-based computational hemodynamics study of the systolic anterior motion of the mitral valve, *Computers in Biology and Medicine* 123 (2020) 103922.
- [46] F. Dassi, D. Mora, C. Reales, I. Velásquez, A virtual element method on polyhedral meshes for the sixth-order elliptic problem, *arXiv preprint arXiv:2211.07953* (2022).
- [47] M. Feder, A. Cangiani, L. Heltai, R3MG: R-tree based agglomeration of polytopal grids with applications to multilevel methods, *arXiv preprint arXiv:2404.18505* (2024).
- [48] P. F. Antonietti, N. Farenga, E. Manuzzi, G. Martinelli, L. Saverio, Agglomeration of polygonal grids using graph neural networks with applications to multigrid solvers, *Computers & Mathematics with Applications* 154 (2024) 45–57.
- [49] A. Quarteroni, L. Dede’, A. Manzoni, C. Vergara, *Mathematical modelling of the human cardiovascular system: data, numerical approximation, clinical applications*, Vol. 33, Cambridge University Press, 2019.
- [50] M. Hirschhorn, V. Tchantchaleishvili, R. Stevens, J. Rossano, A. Throckmorton, Fluid–structure interaction modeling in cardiovascular medicine—a systematic review 2017–2019, *Medical engineering & physics* 78 (2020) 1–13.
- [51] M. Bucelli, A. Zingaro, P. C. Africa, I. Fumagalli, L. Dede’, A. Quarteroni, A mathematical model that integrates cardiac electrophysiology, mechanics, and fluid dynamics: Application to the human left heart, *International Journal for Numerical Methods in Biomedical Engineering* 39 (3) (2023) e3678.
- [52] S. Budday, G. Sommer, J. Haybaeck, P. Steinmann, G. A. Holzapfel, E. Kuhl, Rheological characterization of human brain tissue, *Acta biomaterialia* 60 (2017) 315–329.

- [53] P. Antonietti, I. Mazzieri, High-order discontinuous Galerkin methods for the elastodynamics equation on polygonal and polyhedral meshes, *Computer Methods in Applied Mechanics and Engineering* 342 (2018) 414–437.